

# The scattering of Ly $\alpha$ radiation in the intergalactic medium: numerical methods and solutions

Jonathan Higgins, Avery Meiksin

*SUPA\*, Institute for Astronomy, University of Edinburgh, Blackford Hill, Edinburgh EH9 3HJ, UK*

29 June 2012

## ABSTRACT

Two methods are developed for solving the steady-state spherically symmetric radiative transfer equation for resonance line radiation emitted by a point source in the Intergalactic Medium, in the context of the Wouthuysen-Field mechanism for coupling the hyperfine structure spin temperature of hydrogen to the gas temperature. One method is based on solving the ray and moment equations using finite differences. The second uses a Monte Carlo approach incorporating methods that greatly improve the accuracy compared with previous approaches in this context. Several applications are presented serving as test problems for both a static medium and an expanding medium, including inhomogeneities in the density and velocity fields. Solutions are obtained in the coherent scattering limit and for Doppler RII redistribution with and without recoils. We find generally that the radiation intensity is linear in the cosine of the azimuthal angle with respect to radius to high accuracy over a broad frequency region across the line centre for both linear and perturbed velocity fields, yielding the Eddington factors  $f_\nu \simeq 1/3$  and  $g_\nu \simeq 3/5$ . The radiation field produced by a point source divides into three spatial regimes for a uniformly expanding homogeneous medium. The regimes are governed by the fraction of the distance  $r$  from the source in terms of the distance  $r_*$  required for a photon to redshift from line centre to the frequency needed to escape from the expanding gas. For a standard cosmology, before the Universe was reionized  $r_*$  takes on the universal value independent of redshift of 1.1 Mpc, depending only on the ratio of the baryon to dark matter density. At  $r/r_* < 1$ , the radiation field is accurately described in the diffusion approximation, with the scattering rate declining with the distance from the source as  $r^{-7/3}$ , except at  $r/r_* \ll 1$  where frequency redistribution nearly doubles the mean intensity around line centre. At  $r/r_* > 1$ , the diffusion approximation breaks down and the decline of the mean intensity near line centre and the scattering rate approach the geometric dilution scaling  $1/r^2$ . The mean intensity and scattering rate are found to be very sensitive to the gradient of the velocity field, growing exponentially with the amplitude of the perturbation as the limit of a vanishing velocity gradient is approached near the source. We expect the 21cm signal from the Epoch of Reionization to thus be a sensitive probe of both the density and the peculiar velocity fields.

The solutions for the mean intensity are made available in machine-readable format.

**Key words:** atomic processes – cosmology: theory – line: formation – radiative transfer – radio lines: general – scattering

## 1 INTRODUCTION

The nature of formation of the first radiating objects in the Universe is one of the paramount unsolved problems in cosmological structure formation. Searches for the earliest galaxies have broken the spectroscopically confirmed red-

shift barrier of  $z = 7$  (Vanzella et al. 2011; Ono et al. 2012; Schenker et al. 2012), with plausible candidates identified photometrically up to  $z \lesssim 9$  (McLure et al. 2011), and possibly as high as  $z \simeq 10$  (Bouwens et al. 2011). These systems may well reside within the Epoch of Reionization (EoR) of hydrogen, as Cosmic Microwave Background (CMB) measurements suggest the epoch, if a sudden event, occurred at  $z_r = 10.4 \pm 1.2$  ( $1\sigma$ ) (Komatsu et al. 2011). If so, 21cm

\* Scottish Universities Physics Alliance

emission from the diffuse Intergalactic Medium (IGM) would become visible near this same epoch, as the same sources would provide sufficient UV continuum to excite the line through the Wouthuysen-Field effect (WFE) (Wouthuysen 1952; Field 1958; Madau et al. 1997).

The prospect of discovering the EoR through the associated 21cm signature from the diffuse IGM has inspired the development of a new generation of radio telescopes, such as the LOw Frequency Array (LOFAR)<sup>1</sup>, upgrades to the Giant Metrewave Radio Telescope (GMRT)<sup>2</sup>, the Murchison Widefield Array (MWA)<sup>3</sup>, the Primeval Structure Telescope/21 Centimeter Array (PaST/21CMA)<sup>4</sup>, the Precision Array to Probe EoR (PAPER)<sup>5</sup>, and a possible Square Kilometre Array (SKA)<sup>6</sup>. A recent review of this rapidly growing area is provided by Pritchard & Loeb (2011).

The interpretation of the signal will require modelling the radiative transfer of the Lyman resonance line photons, primarily Ly $\alpha$ , that drive the WFE. Most estimates have presumed a homogeneous expanding medium. Early modelling neglected the effects of atomic recoil and of spatial diffusion about the emitting sources, assuming the sources were homogeneously and isotropically distributed throughout the Universe (Field 1959a; Madau et al. 1997). Allowing for recoil somewhat suppresses the Ly $\alpha$  photon scattering rate by an amount depending on the local temperature and expansion rate of the IGM (Chen & Miralda-Escudé 2004; Furlanetto & Pritchard 2006). Using Monte Carlo solutions to the radiative transfer equation to include spatial diffusion, it was found that near an emitting source the scattering rate varies as  $r^{-7/3}$  (Chuzhoy & Zheng 2007; Semelin et al. 2007), more rapidly than the geometric dilution factor  $r^{-2}$  predicted without spatial diffusion. It will be shown below that the steeper dependence arises generally over all distances for which the radiative transfer of the Ly $\alpha$  photons may be treated in the diffusion approximation.

In reality the IGM is clumpy, with structures breaking away from the cosmological expansion. Simple analytic estimates suggest that the scattering rate will be substantially modified not only by density and temperature fluctuations, but by gradients in the velocity field of the gas around individual sources (Higgins & Meiksin 2009). More sophisticated methods are required for accurate solutions of the spatial and frequency dependent radiative transfer equation. Monte Carlo codes were developed for this purpose (Zheng & Miralda-Escudé 2002; Tasitsiomi 2006; Chuzhoy & Zheng 2007; Semelin et al. 2007). The method has recently been applied to estimate the expected cosmological 21cm signal (Baek et al. 2009; Vonlanthen et al. 2011). A difficulty with the Monte Carlo technique is the limited resolution imposed by the restricted number of photon packets that may be practically followed. An alternative grid-based method for solving the spherically-symmetric radiative transfer equation in the Eddington approximation has been developed by Roy et al. (2009b) for linear flow fields.

Scattering in the deuterium Ly $\alpha$  resonance and the ad-

dition of Ly $\alpha$  photons produced in radiative cascades following the scattering of higher order Lyman resonance line photons will modify the Ly $\alpha$  mean intensity and scattering rate near a source. As these are smaller, secondary effects (Chuzhoy & Zheng 2007; Semelin et al. 2007), they are not included in this paper.

A further complication is the time required to establish a steady-state radiation field. The Ly $\alpha$  photon scattering rate scales like  $t_s \simeq 3.2n_{\text{HI}}^{-1}T^{1/2}$  s for a gas with neutral hydrogen density  $n_{\text{HI}}$  and temperature  $T$ . Time-dependent radiative transfer computations suggest it may take  $10^4 - 10^{12}$  scatterings to establish a steady-state radiation field, depending on the internal structure of the scattering system, including internal velocity gradients (Higgins & Meiksin 2009; Roy et al. 2009a). Timescales of  $10^6 - 10^9$  yr, comparable to or longer than the evolutionary timescale of starbursts and quasars, may be required for structures that have broken away from the cosmic expansion, particularly in the presence of substantial x-ray heating.

In this paper, we present two algorithms for solving the radiative transfer equation of an inhomogeneous medium, one based on finite-differences on a grid and the second Monte Carlo based. The grid-based method combines solutions to the ray equation and the moment equation based on the method of Mihalas et al. (1975, 1976, 1977). The inclusion of solutions to the ray equation allows the sequence of moment equations to be closed without imposing the Eddington approximation. Since the method was developed for stellar atmospheres, modifications to the approach are described necessary to adapt the method to the problem of a source in the IGM. The method has a few restrictions: 1. it is implemented assuming spherical symmetry, 2. it assumes a steady state, and 3. it requires the velocity field around the source to be monotonically increasing or decreasing. In practice the latter is not a severe restriction because the peculiar velocity field only modulates the Hubble flow except within the turnaround radius very near the source. The assumption of spherical symmetry may not be very restrictive either, since the photons do not diffuse very far compared with the coherence length of cosmological structures. A solution along a ray in a 3D computation may therefore not differ much from that assuming the medium is isotropic with the radial properties of the ray. We are not able to test this, however, without a fully 3D solution to the radiative transfer equation, which is beyond the scope of this paper. As noted above, situations may arise in which the steady-state approximation will break down.

The Monte Carlo method is similar to existing algorithms for resonance line radiation, but with two improvements. It incorporates RII frequency redistribution by interpolating on the RII redistribution function rather than directly computing collisions with atoms. This improves the speed of the computations by a factor of a few, but at the cost of requiring a frequency grid tailored to the particular problem. The second improvement is to compile the specific mean intensity based on the path lengths traversed by the photon packets rather than on frequency and position bin crossings. This improvement is general and substantially reduces the noise in the specific mean intensity for a fixed number of photon packets. The method also serves as an independent check on the solutions obtained through the ray and moments method.

<sup>1</sup> www.lofar.org

<sup>2</sup> gmrt.ncra.tifr.res.in

<sup>3</sup> www.haystack.mit.edu/ast/arrays/mwa

<sup>4</sup> web.phys.cmu.edu/~past

<sup>5</sup> astro.berkeley.edu/~dbacker/eor

<sup>6</sup> www.skatelescope.org

The paper is organised as follows. The basic framework used to solve the radiative transfer equation in spherical symmetry using the ray and moments method on a grid is presented in the next section. In Section 3, we summarise the Monte Carlo method developed. We present the results of validation tests of both methods against analytic solutions for a homogeneous medium in Section 4. Both methods are applied to scattering problems in an inhomogeneous medium in Section 5. A summary and conclusions follow. Details of the source term used for the ray and moment solution are provided in Appendix A. The Monte Carlo method is described in Appendix B. The solution to the radiative transfer problem for a point continuum source in a uniformly expanding homogeneous medium in the diffusion approximation is derived in Appendix C. Tables of solutions to a test suite of problems using the ray and moments method are provided online in machine-readable format, as summarised in Appendix D.

## 2 NUMERICAL RADIATIVE TRANSFER IN SPHERICAL SYMMETRY I: RAY AND MOMENT EQUATIONS

### 2.1 Methodology

We developed a grid-based method for obtaining precise numerical solutions to the radiative transfer equation in spherical symmetry based on the method of Mihalas et al. (1975, 1976, 1977). This method was developed for stellar atmospheres and consequently we have had to formulate the boundary conditions for a non-blackbody source. Here we provide a summary of our implementation.

The radiative transfer equation for the specific intensity  $I_\nu$  in the comoving frame for a spherically symmetric scattering medium with specific volume emissivity  $\eta_\nu$ , inverse attenuation length  $\chi_\nu$  and radial velocity  $V(r)$  is given by (Mihalas 1978)

$$\mu \frac{\partial I_\nu}{\partial r} + \frac{1 - \mu^2}{r} \frac{\partial I_\nu}{\partial \mu} - \alpha(r) [1 - \mu^2 + \mu^2 \beta(r)] \frac{\partial I_\nu}{\partial \nu} = -\chi_\nu I_\nu + \eta_\nu, \quad (1)$$

where  $\alpha(r)$  and  $\beta(r)$  are given by

$$\alpha(r) \equiv (\nu_0/c) \frac{V(r)}{r}, \quad (2)$$

$$\beta(r) \equiv \frac{d \ln V(r)}{d \ln r}, \quad (3)$$

and  $\mu$  is the cosine of the inclination relative to the radial direction of the radiation field described by  $I_\nu(r, \mu)$ , and  $\nu_0$  is the resonance line frequency. We limit our study to expanding velocity fields  $V(r)$  satisfying  $V(r) > 0$  and  $V'(r) > 0$  for all  $r$ . (The method also may be applied to a monotonically decreasing radial velocity field. Non-monotonic fields would require combining solutions from piecewise monotonic fields.) The method requires solving a system of angular moment equations derived from equation (1), together with a solution of equation (1) itself along a specific set of rays. The approach is to solve the ray and moment equations simultaneously, iterating between the two until adequate convergence is achieved. In solving the ray equations, we treat the angular dependence of the radiation field exactly, however we assume that the source function  $S_\nu(r)$  is a known

quantity. In solving the moment equations we assume angular information in the form of variable Eddington factors in order to close the system of equations, however we are able to treat the dependence of the source function on the radiation field exactly. The iteration procedure is implemented by first seeking a solution to the ray equations utilising an estimate of the source function, before evaluating the variable Eddington factors from the ray solution and using them to obtain a solution to the moment equations. It may then be necessary to improve on the estimate of the Eddington factors by repeating the ray solution steps with an improved source function estimate derived from the moment solution, a process that may be iterated until convergence. At each step the solution of the ray/moment equations is obtained from finite-difference forms which are written as matrix equations. The matrix equations are provided by Higgins (2012). We next outline the method in greater detail.

### 2.2 Ray Equations

In spherical symmetry the radiation field may be described as a function of radius  $r$  and the angle  $\theta$  to the local radius vector. A pair of variables more appropriate for describing the properties of the radiation field along a particular ray is given by the impact parameter,  $p \equiv r \sin \theta = r(1 - \mu^2)^{1/2}$ , and the distance along the ray from the point of closest approach to the origin,  $z \equiv r \cos \theta = r\mu$  where  $\mu \equiv \cos \theta$ . Radiative transfer along a ray of a given impact parameter  $p$  is described by the equations

$$\pm \frac{\partial I_\nu^\pm(p, z)}{\partial z} - \alpha(r) [1 - \mu^2 + \beta(r)\mu^2] \frac{\partial I_\nu^\pm(p, z)}{\partial \nu} = \eta_\nu(r) - \chi_\nu(r) I_\nu^\pm(p, z) \quad (4)$$

where  $I_\nu^\pm(p, z)$  is the specific intensity of radiation a distance  $z$  along the ray, in the direction of increasing  $z$  for  $I_\nu^+$  or decreasing  $z$  for  $I_\nu^-$ . In spherical symmetry the intensities are equivalently written as  $I_\nu^+(p, z) = I_\nu(r, \mu)$  and  $I_\nu^-(p, z) = I_\nu(r, -\mu)$  where  $\mu > 0$ . It is convenient to work with the following linear combinations of the specific intensities:

$$u_\nu(p, z) \equiv \frac{1}{2} [I_\nu^+(p, z) + I_\nu^-(p, z)], \quad (5)$$

$$v_\nu(p, z) \equiv \frac{1}{2} [I_\nu^+(p, z) - I_\nu^-(p, z)]. \quad (6)$$

We may obtain equations for the development of  $u_\nu$  and  $v_\nu$  along a ray by summing and differencing, respectively, the transfer equations for  $I_\nu^+$  and  $I_\nu^-$ . If we then change variables to the optical depth along the ray, defined by  $d\tau_\nu = -\chi_\nu dz$ , we arrive at

$$\frac{\partial u_\nu(z)}{\partial \tau_\nu} + \gamma_\nu(z) \frac{\partial v_\nu(z)}{\partial \nu} = v_\nu(z), \quad (7)$$

$$\frac{\partial v_\nu(z)}{\partial \tau_\nu} + \gamma_\nu(z) \frac{\partial u_\nu(z)}{\partial \nu} = u_\nu(z) - S_\nu(r), \quad (8)$$

where we have defined coefficients

$$\gamma_\nu(z) \equiv \frac{\alpha(r)}{\chi_\nu(r)} [1 - \mu^2 + \beta(r)\mu^2], \quad (9)$$

and  $S_\nu(r) \equiv \eta_\nu(r)/\chi_\nu(r)$  is the source function of the scattering medium, which is here assumed to be a known function.

We specify a maximum and minimum radius of the spherical system under consideration, given respectively by  $R$  and  $R_C$ . (The subscript ‘C’ here denotes the ‘core’, the central object/region of the spherical system.) The boundary conditions are:

(a)  $r = R, z = z_{\max}$ : We assume that  $R$  has been chosen to be sufficiently large that there is no radiation scattered back into the system from this radius, i.e.  $I_\nu(R, \mu) = 0$  for  $\mu < 0$ , and thus along the ray  $I_\nu^-(p, z_{\max}) = 0$  where  $z_{\max} = (R^2 - p^2)^{1/2}$ . From the definitions given by equations (5) and (6) we see that  $v_\nu(z_{\max}) = u_\nu(z_{\max})$ . We arrive at a suitable boundary condition by substituting this into equation (7):

$$\frac{\partial u_\nu(z_{\max})}{\partial \tau_\nu} + \gamma_\nu(z_{\max}) \frac{\partial u_\nu(z_{\max})}{\partial \nu} = u_\nu(z_{\max}). \quad (10)$$

(b)  $r = R_C, z = z_{\min}$ : For the inner boundary condition we need to consider two distinct cases applicable depending on the impact parameter of the ray chosen:

(i)  $p \geq R_C$ : We compute the radiative transfer along the ray which is considered to originate from  $z_{\min} = 0$ . Due to the symmetry of the problem we may impose  $I_\nu^+ = I_\nu^-$  at  $z = 0$  and therefore  $v_\nu(p, z_{\min}) = 0$ . Thus equation (7) becomes

$$\frac{\partial u_\nu(z = 0)}{\partial \tau_\nu} = 0. \quad (11)$$

(ii)  $p < R_C$ : The ray intersects the core, and the minimum value of  $z$  denotes the distance along the ray at which the intersection occurs:  $z_{\min} = (R_C^2 - p^2)^{1/2}$ . The boundary condition is written as:

$$\frac{\partial u_\nu(z_{\min})}{\partial \tau_\nu} = v_\nu(z_{\min}) - \gamma_\nu(z_{\min}) \frac{\partial v_\nu(z_{\min})}{\partial \nu} \quad (12)$$

where we assume the function  $v_\nu(R_C, \mu)$  is known.

If the optical depth at the core radius is sufficiently high then the intensity will display the angular behaviour found in the diffusion limit,  $I_\nu(R_C, \mu) = J_{\nu,C} + 3H_{\nu,C}\mu$ , where  $J_{\nu,C}$  is the core mean intensity and  $H_{\nu,C}$  is the core flux. From the definition of  $v_\nu$  and the equation for  $I_\nu(R_C, \mu)$  we find

$$v_\nu(R_C, \mu) = 3|\mu|H_{\nu,C}. \quad (13)$$

In this limit we should take  $H_{\nu,C}$  to be a solution valid in the diffusion limit, if such a solution is known. If the optical depth at the core radius is significantly less than unity then we may assume a free-streaming boundary condition of the form

$$v_\nu(R_C, \mu) = H_{\nu,C} \delta_D(\mu - 1) \quad (14)$$

where  $\delta_D$  is the Dirac delta function and thus the radiation field is directed radially outward from the source ( $\mu = 1$ ). The flux and the mean intensity are equal in this limit and trivially related to the source spectrum  $L_\nu$  by  $H_{\nu,C} = J_{\nu,C} = L_\nu / (4\pi R_C)^2$ .

The medium is subject to a radial velocity  $V(r)$  that satisfies  $V(r) \geq 0$ ,  $dV/dr \geq 0$  for all  $r$ ; this ensures that  $\gamma_\nu \geq 0$  for all  $(p, z)$ . From subsequent analysis of the characteristics of the system given by equations (7) and (8), we need to enforce an initial condition at high frequency; we denote this frequency by  $\nu_{\max}$ . The properties of  $V(r)$  tell us that every point moves away from every other point and all radiation intercepted at a specific point from elsewhere in the system is redshifted. From this argument we see that if  $\nu_{\max}$  lies sufficiently blueward of the local line profile, such

that no line photons ever reach  $\nu_{\max}$ , then

$$I_\nu(r, \mu)|_{\nu_{\max}} = 0, \quad (15)$$

$$\left. \frac{\partial I_\nu(r, \mu)}{\partial \nu} \right|_{\nu_{\max}} = 0. \quad (16)$$

Note that equation (15) holds for a system interacting with resonance-line photons only, while the condition of zero frequency gradient given by equation (16) also applies in the more general case where we allow for continuum radiation as the continuum varies slowly with frequency. The equations are solved ray-by-ray, frequency-by-frequency using a matrix equation approach (Mihalas et al. 1975).

### 2.3 Moment Equations

From equation (1) we derive angular moment equations with respect to  $\mu$ . We obtain the following for the zeroth- and first-order moment equations:

$$\frac{1}{r^2} \frac{\partial(r^2 H_\nu)}{\partial r} - \alpha \left[ \frac{\partial(J_\nu - K_\nu)}{\partial \nu} + \beta \frac{\partial K_\nu}{\partial \nu} \right] = \eta_\nu - \chi_\nu J_\nu, \quad (17)$$

$$\frac{\partial K_\nu}{\partial r} + \frac{3K_\nu - J_\nu}{r} - \alpha \left[ \frac{\partial(H_\nu - N_\nu)}{\partial \nu} + \beta \frac{\partial N_\nu}{\partial \nu} \right] = -\chi_\nu H_\nu \quad (18)$$

where we have made use of the definitions of the first four moments of the specific intensity:

$$[J_\nu, H_\nu, K_\nu, N_\nu] = \frac{1}{2} \int_{-1}^1 d\mu I_\nu(\mu) [1, \mu, \mu^2, \mu^3]. \quad (19)$$

It is necessary to utilise additional constraints relating the four angular moments of the radiation intensity to obtain a closed system of moment equations. We assume a relationship between the moments dictated by the ‘variable Eddington factor’  $f_\nu(r)$ , defined as:

$$f_\nu(r) \equiv \frac{K_\nu(r)}{J_\nu(r)}. \quad (20)$$

We define a further variable Eddington factor  $g_\nu(r)$  linking the first and third order moments  $H_\nu(r)$  and  $N_\nu(r)$ :

$$g_\nu(r) \equiv \frac{N_\nu(r)}{H_\nu(r)}. \quad (21)$$

The values of  $f_\nu(r)$  and  $g_\nu(r)$  are dependent on the angular character of the radiation field at  $(r, \nu)$ , and are determined by the solution of the ray equations.

We estimate the  $n$ th-order angular moments of the intensity  $I_\nu(r, \mu)$  for  $n = 0, 1, 2, 3$  which may be rewritten as

$$J_\nu(r) \equiv \frac{1}{2} \int_{-1}^1 I_\nu(r, \mu) d\mu = \int_0^1 u_\nu(r, \mu) d\mu, \quad (22)$$

$$H_\nu(r) \equiv \frac{1}{2} \int_{-1}^1 \mu I_\nu(r, \mu) d\mu = \int_0^1 \mu v_\nu(r, \mu) d\mu, \quad (23)$$

$$K_\nu(r) \equiv \frac{1}{2} \int_{-1}^1 \mu^2 I_\nu(r, \mu) d\mu = \int_0^1 \mu^2 u_\nu(r, \mu) d\mu, \quad (24)$$

$$N_\nu(r) \equiv \frac{1}{2} \int_{-1}^1 \mu^3 I_\nu(r, \mu) d\mu = \int_0^1 \mu^3 v_\nu(r, \mu) d\mu \quad (25)$$

where the second equality in each case is reached by utilising the definitions of  $u_\nu(r, \mu)$  and  $v_\nu(r, \mu)$  in terms of  $I_\nu(r, \mu)$  and  $I_\nu(r, -\mu)$ . We evaluate the integrals by a gaussian quadrature formula where the integral over  $\mu$  is replaced by a sum over different impact parameter values. For numerical accuracy, we split the integral into the domains  $0 < \mu < \mu_C$  and  $\mu_C < \mu < 1$ , where  $\mu_C = (r^2 + R_C^2)^{1/2}/r$  corresponds to the core radius opening angle subtended at  $r$ . We then obtain  $f_\nu(r)$  and  $g_\nu(r)$  by evaluating the relevant ratios as described in equations (20) and (21).

We define the ‘sphericity factor’  $q_\nu(r)$  by the relation (Auer 1971)

$$\frac{\partial \ln(r^2 q_\nu)}{\partial r} = \frac{3f_\nu - 1}{f_\nu r}. \quad (26)$$

We calculate  $q_\nu(r)$  given the variable Eddington factor  $f_\nu(r)$  and the arbitrary normalisation  $q_\nu(R_C) = 1$  from

$$q_\nu(r) = \left(\frac{r}{R_C}\right)^{-2} \exp \left[ \int_{R_C}^r \frac{3f_\nu(r') - 1}{r' f_\nu(r')} dr' \right]. \quad (27)$$

This quantity allows us to make a change of variable in the radial derivative to the dimensionless quantity  $X_\nu(r)$  defined through

$$dX_\nu(r) = -\chi_\nu(r) q_\nu(r) dr. \quad (28)$$

The terms on the LHS of equations (17) and (18) may then be expressed as

$$\frac{\partial(r^2 H_\nu)}{\partial r} = -q_\nu \chi_\nu \frac{\partial(r^2 H_\nu)}{\partial X_\nu}, \quad (29)$$

$$\frac{\partial(f_\nu J_\nu)}{\partial r} + \frac{3f_\nu - 1}{r} J_\nu = -r^{-2} \chi_\nu \frac{\partial(r^2 q_\nu f_\nu J_\nu)}{\partial X_\nu}. \quad (30)$$

These relations and the definitions of  $f_\nu$  and  $g_\nu$  may be used to recast the zeroth and first order moment equations as

$$q_\nu \frac{\partial(r^2 H_\nu)}{\partial X_\nu} + \Gamma_\nu \left[ \frac{\partial(1 - f_\nu)r^2 J_\nu}{\partial \nu} + \beta \frac{\partial(f_\nu r^2 J_\nu)}{\partial \nu} \right] = r^2 (J_\nu - S_\nu), \quad (31)$$

$$\frac{\partial(f_\nu q_\nu r^2 J_\nu)}{\partial X_\nu} + \Gamma_\nu \left[ \frac{\partial(1 - g_\nu)r^2 H_\nu}{\partial \nu} + \beta \frac{\partial(g_\nu r^2 H_\nu)}{\partial \nu} \right] = r^2 H_\nu \quad (32)$$

where  $\Gamma_\nu(r) = \alpha(r)/\chi_\nu(r)$  and once again  $S_\nu(r) = \eta_\nu(r)/\chi_\nu(r)$  is the source function, although in solving the moment equations we account for the dependence of the source function on the radiation field and will not assume a given estimate as for the ray equations. Assuming the isotropic forms of the opacity and emissivity for resonance-line scattering, a good approximation in the comoving frame, the source function is given by

$$S_\nu(r) \equiv \frac{\eta_\nu(r)}{\chi_\nu(r)} = \frac{1}{\varphi(\nu, r)} \int R(\nu', \nu, r) J_{\nu'}(r) d\nu' \quad (33)$$

where we have allowed for the redistribution function and absorption profile to vary with radius due to any variation in the temperature profile of the medium,  $T(r)$ . The integral is expanded as a numerical quadrature sum as described in Appendix A.

We note that boundary conditions appropriate for the

solution of the system of moment equations are given by taking equation (32) and (i) directly specifying  $H_\nu(R_C) = H_{\nu,C}$  for the inner boundary, and (ii) at the outer boundary, specifying the ratio  $h_\nu = H_\nu(R)/J_\nu(R)$  as calculated from the formal ray solution similarly to the variable Eddington factor computation. The equations are solved using the Feautrier matrix equation approach (Mihalas et al. 1976).

### 3 NUMERICAL RADIATIVE TRANSFER IN SPHERICAL SYMMETRY II: MONTE CARLO

We implement a Monte Carlo method to obtain the mean intensity of Ly $\alpha$  photons and the corresponding scattering rate in a spherically symmetric medium with a general radial velocity profile. It differs from existing schemes in a few aspects, leading to an order of magnitude increase in speed for a given accuracy, so we describe it in some detail. In addition to the assumption of spherical symmetry, we sample the redistribution function directly and compute the energy density based on the path lengths traversed by the photons.

Here we summarise the method developed and refer the reader to Appendix B for details. We impose a grid of ND radius values  $\{r_{ND}, r_{ND-1}, \dots, r_1\}$  where  $r_{ND}$  is the innermost radius at which we compute the intensity and  $r_1$  is the radius of the outer boundary. We assume the neutral hydrogen is confined to  $r < r_1$  and thus there is no scattering for  $r > r_1$ . The algorithm, in outline, is as follows:

(i) A photon packet is emitted at some radius  $r_{em}$  and comoving frequency  $x_{em}$  determined from the properties of the source. The packet is assigned a direction typically taken to be isotropic, i.e.  $\mu_{em} = 2R - 1$ , and an optical depth  $\tau = -\ln R$ , where  $R$  is a random deviate uniformly distributed over  $0 \leq R \leq 1$  (drawn separately for  $\mu_{em}$  and  $\tau$ ), after which it will be scattered by the hydrogen.

(ii) We follow the potential path of the photon packet defined by  $r_{em}$  and  $\mu_{em}$ , originating at  $\lambda = 0$ , where  $\lambda$  describes the path length, to the first intersection with a shell boundary and compute the distance  $\lambda_s$  and optical depth  $\tau_s$  from equations (B1) and (B5), respectively.

(iii) If  $\tau > \tau_s$  then the photon packet will cross the boundary, if not we skip to (iv). We update the position by setting  $(\lambda + \lambda_s) \rightarrow \lambda$  and compute the comoving frequency between the boundaries using equations (B2) and (B3). We bin the frequency and add the appropriate  $\delta\lambda(s)$  to the sum in equation (B7) for the corresponding frequency bin(s) and volume cell. We take  $(\tau - \tau_s) \rightarrow \tau$  and determine values of  $\lambda_s$  and  $\tau_s$  from the current position to the next shell boundary along the path; this step is repeated until  $\tau_s > \tau$  indicating the packet scatters before reaching the next boundary. If the packet crosses the boundary at  $r_1$  then it escapes the H I medium and cannot be scattered back to  $r < r_1$ . In this case we return to step (i) for a new photon packet if required.

(iv) We assume the packet travels a further distance  $\Delta\lambda = (\tau/\tau_s)\lambda_s$  along the path and add  $\delta\lambda = \Delta\lambda$  to the sum to compute  $J_\nu(r)$  for the appropriate volume cell, where again the comoving frequency is binned along this section of path and  $\Delta\lambda$  must be broken into multiple values of  $\delta\lambda$  if the range in comoving frequency is not contained in a single frequency bin. We obtain the total distance travelled by the

photon packet from  $\mathbf{r}_{\text{em}}$  before scattering from  $\lambda + \Delta\lambda \rightarrow \lambda$ . The radius  $r$  is updated according to equation (B6) with  $\lambda$  in place of  $\lambda_{\text{max}}$ . The comoving frequency from which the packet is scattered,  $x'$ , is determined from equation (B3) with  $\mu(r) = (\mu_{\text{em}} r_{\text{em}} + \lambda)/r$ .

(v) The photon packet is re-emitted at  $r_{\text{em}} = r$  with a comoving frequency  $x_{\text{em}} = x_{\text{em}}(x', T)$  determined from the appropriate redistribution function, e.g. type II redistribution (RII) with or without recoil, or even coherent scattering ( $x_{\text{em}} = x'$ ). We assign an isotropically distributed direction  $\mu_{\text{em}} = 2R - 1$  and optical depth to next scatter  $\tau = -\ln R$ . We return to step (ii).

This sequence of steps is repeated for as many photon packets as are necessary to reduce the statistical noise in  $J_\nu(r)$  to acceptable levels. The normalisation in equation (B7) is enforced by relating the  $\Delta t$  for the Monte Carlo simulation to the number of photons followed, using the assumed physical properties of the source as described later for the particular examples we study.

## 4 TEST PROBLEMS FOR A HOMOGENEOUS MEDIUM

### 4.1 Static Sphere

Dijkstra et al. (2006) obtained an analytic solution for the mean intensity of Ly $\alpha$  radiation in a static uniform sphere allowing for RII frequency redistribution analogous to that for a plane-parallel slab (Harrington 1973). They considered a system of radius  $R$  and line-centre opacity  $\kappa_0$ , with a source term of unit strength, frequency distribution  $\phi(x)$  and arbitrary radial distribution  $j(r)$ , and assumed an outer boundary condition applicable in the Eddington limit:

$$H_\nu(r)|_R = \frac{1}{2} J_\nu(r)|_R. \quad (34)$$

They found the solution

$$J(x, r) = \frac{\sqrt{6\pi}\kappa_0}{16\pi^2 R} \sum_{n=1}^{\infty} Q_n \frac{\sin(\lambda_n r)}{\lambda_n r} \exp\left(-\sqrt{\frac{2\pi}{27}} \frac{\lambda_n}{a\kappa_0} |x^3|\right), \quad (35)$$

where the factors  $\{Q_n\}$  are related to the radial distribution function  $j(r)$  by

$$Q_n \equiv \int_0^R 4\pi r^2 \frac{\sin(\lambda_n r)}{r} j(r) dr, \quad (36)$$

and the radial ‘eigenvalues’  $\{\lambda_n\}$  are constrained by the outer boundary condition to the frequency-dependent values:

$$\lambda_n(x) \approx \frac{n\pi}{R} \left[1 - \frac{1}{1 + 1.5\pi^{1/2}\kappa_0 R\phi(x)}\right]. \quad (37)$$

In the diffusion approximation assumed by Dijkstra et al. (2006), the radiation flux is related to the average intensity by the first order angular moment equation,  $H(r, x) = -1/(3\chi_\nu)\partial J(r, x)/\partial r$  where the opacity is  $\chi_\nu = \sqrt{\pi}\kappa_0\phi(x)$ . The corresponding solution for the flux, derived by taking

the radial derivative, is

$$H(x, r) = \frac{\sqrt{6}}{48\pi^2 R\phi(x)} \sum_{n=1}^{\infty} \frac{Q_n}{\lambda_n} \left[ \left( \frac{\sin(\lambda_n r)}{r^2} - \frac{\lambda_n \cos(\lambda_n r)}{r} \right) \times \exp\left(-\sqrt{\frac{2\pi}{27}} \frac{\lambda_n}{a\kappa_0} |x^3|\right) \right]. \quad (38)$$

Dijkstra et al. (2006) suggest a source term describing a thin shell at some source radius  $r_s$  with the radial distribution and corresponding  $Q_n$  values

$$j(r) = \frac{1}{\sqrt{\pi}\kappa_0} \frac{\delta_D(r - r_s)}{4\pi r^2} \implies Q_n = \frac{1}{\sqrt{\pi}\kappa_0} \frac{\sin(\lambda_n r_s)}{r_s}, \quad (39)$$

which corresponds to a point source in the limit  $r_s \rightarrow 0$  or  $r \gg r_s$ . The source term is  $S(x, r) = \chi_\nu j(r)/(4\pi)$ . The normalisation ensures the condition  $\int dx \int dV \oint d\Omega S(x, r) = 1$  is met.

We now consider the application of the moment and ray equation solution methods to this particular problem. The inner boundary condition is applied at a ‘core radius’  $R_C$ . As the moment equations that we solve do not account for a source term, it is important that the source is contained within the core,  $R_C > r_s$ , such that the properties of the source are described by the core boundary condition. This boundary condition is given by assuming the diffusion limit  $v_\nu(R_C, \mu) = 3|\mu|H_\nu(R_C)$  in solving the ray equations. In both cases we take the analytic solution equation (38) for  $H_\nu(R_C)$  with the  $Q_n$  coefficients given by equation (39). In estimating the source function assumed when solving the ray equations, it is sufficient to evaluate the integral equation (33) using the analytic solution equation (35) as an estimate of the mean intensity, while the source function in the moment equations follows from equations (A4) and (A6) with  $\epsilon = 0$  for the coefficients. We take a linear grid in radius spanning  $[R_C, R]$  and a linear grid of frequency values  $\{x_k\}$  spanning the range over which the analytic solution is non-negligible. As a first step we attempt to solve the problem in the Eddington approximation by solving the moment equations with  $f_\nu(r) \equiv 1/3$ .

Examples of the resulting moment equation solution are shown in Fig. 1. We find our results agree with the analytic solution of Dijkstra et al. apart from differences across the line centre in the lower optical depth case; the moment equation solution is the more accurate of the two as the analytic solution is an exact solution in the Eddington approximation only in the limit  $(a\tau_0)^{1/3} \gg 1$ .

A numerical solution without assuming the Eddington approximation may be constructed by solving the moment equations with Eddington factors determined from solving the ray equations as described in Section 2.1. In Fig. 2, we compare the ray/moment equations solutions with the corresponding Monte Carlo solutions. The Monte Carlo solution in the upper panel of Fig. 2 was obtained according to the summed path-length method of Section 3, while in the lower panel we obtained the mean intensity at the outer boundary surface using the definition of specific intensity. The Monte Carlo solutions in each case were normalised by computing the simulation timescale  $\Delta t$  as required by equation (B7) or equation (B8) as  $\Delta t = N/(1 \text{ photon s}^{-1})$ , which follows from the unit source strength imposition. The solutions were ob-

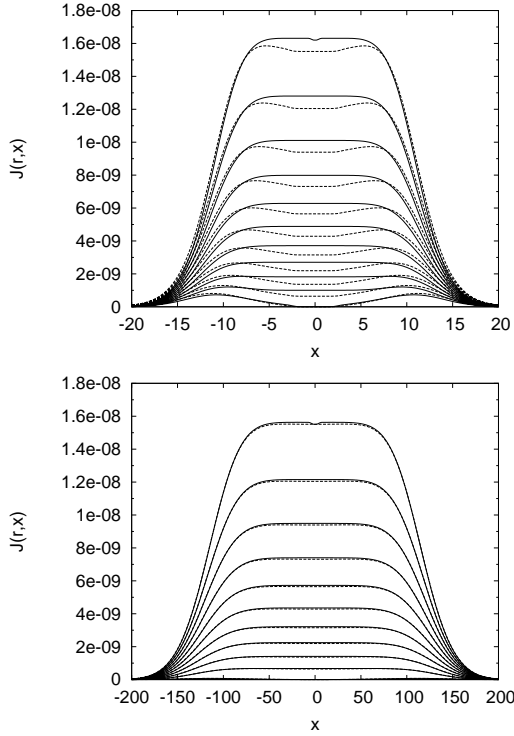


**Figure 1.** The mean intensity  $J(r, x)$  for Ly $\alpha$  RII scattering in a static, uniform sphere in the Eddington approximation. Solutions assume a source radial dependence of the form equation (39) for  $r_S = 5$ , a temperature  $T = 10$  K, and a line-centre opacity  $\kappa_0 = 100$  (upper panel) and  $\kappa_0 = 1.2 \times 10^5$  (lower panel). Frequency profiles are given from  $r = 500$  (highest values of  $J$ ) to  $r = 1000$  (lowest values of  $J$ ) in steps of 50. In each panel we display the solutions of the moment equations in the Eddington approximation (solid line) together with the corresponding analytic solution in the diffusion approximation of Dijkstra et al. (2006) (dashed line).

tained by following  $N = 2 \times 10^5$  photon packets for the case shown in the upper panel, and  $N = 2 \times 10^4$  photon packets for the lower. The frequency redistribution was treated using the lookup table method in the low optical depth case, while in the optically thick case we used the scattering atom velocity method with a bias to skip over core scatterings. From Fig. 2, we find that our ray/moment equation solutions agree closely with the Monte Carlo solutions for both low and high optical depths, with only small deviations from the analytic solution in both cases. We found no significant alterations to the ray/moment solutions upon re-solving the ray and moment equations with an estimated source function obtained from the moment solution, suggesting that for this problem the combined method converges in a single iteration.

#### 4.2 Homogeneous Expanding Medium: Ly $\alpha$ Source

As a simple test of the ray/moment equation and Monte Carlo methods for a non-static, spherically symmetric medium, we use the problem of a Ly $\alpha$  point source in a homogeneous expanding H I medium (Loeb & Rybicki 1999). Loeb & Rybicki added an extra source term  $S(\nu, r)$  to the RHS of equation (1) to model a point source of Ly $\alpha$  photons

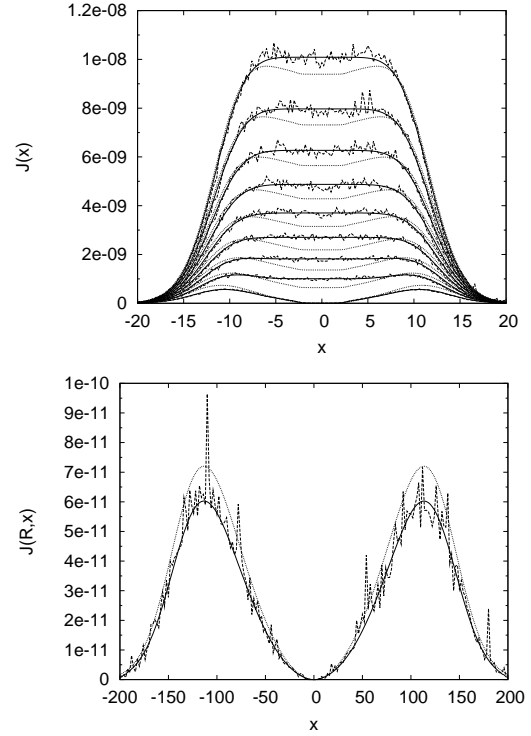


**Figure 2.** The mean intensity  $J(r, x)$  for Ly $\alpha$  RII scattering in a static, uniform sphere. Solutions assume a source radial dependence of the form equation (39) for  $r_S = 5$ , a temperature  $T = 10$  K, and a line-centre opacity  $\kappa_0 = 100$  (upper panel) and  $\kappa_0 = 1.2 \times 10^5$  (lower panel). In the upper panel, frequency profiles are given from  $r = 600$  (highest values of  $J$ ) to  $r = 1000$  (lowest values of  $J$ ) in steps of 50 while we display only  $J(R, x)$  in the lower panel. We compare our ray/moment equation solutions (solid line) with the corresponding Monte Carlo solution (dashed line) and the analytic solution in the diffusion approximation (dotted line). While noisy near line centre, the Monte Carlo solutions agree well with the ray/moment equations solutions in the wings.

at the origin:

$$S(\nu, r) = \dot{N}_\alpha \delta(\nu - \nu_\alpha) \frac{\delta(r)}{(4\pi r)^2}, \quad (40)$$

where  $\dot{N}_\alpha$  is the rate of emission of Ly $\alpha$  photons with frequency  $\nu_\alpha$ . They introduced a characteristic frequency  $\nu_*$ , defined such that photons in the red Lorentz wing with  $\chi_\nu = \eta(\nu - \nu_\alpha)^{-2}$ , where  $\eta \equiv n_H \sigma \Gamma_\alpha / (4\pi^2)$ , accumulate an optical depth of unity in redshifting from the source with frequency  $\nu = \nu_*$  to an observer at infinity:

$$\begin{aligned} \nu_* &\equiv \frac{\eta}{\alpha} = \frac{\sigma \Gamma_\alpha \lambda_\alpha n_H(z)}{4\pi^2 H(z)} \simeq \frac{\sigma \Gamma_\alpha \lambda_\alpha n_H(0)}{4\pi^2 \Omega_m^{1/2} H_0} (1+z)^{3/2} \\ &\simeq 5.52 \times 10^{12} \left( \frac{\Omega_b h}{\Omega_m^{1/2}} \right) (1+z)^{3/2} \text{ Hz} \end{aligned} \quad (41)$$

where we have assumed a neutral medium with  $n_H(z) = n_H(0)(1+z)^3$ ,  $H(z) \simeq H_0 \Omega_m^{1/2} (1+z)^{3/2}$ , as the universe is matter-dominated at the redshifts of interest, and  $\alpha = H(z)\nu_\alpha/c$ . Loeb & Rybicki defined the characteristic radius  $r_*$  as the radius at which a photon free streaming from the

source redshifts from  $\nu_\alpha$  to  $(\nu_\alpha - \nu_*)$ , i.e.  $\alpha r_* = \nu_*$ :

$$r_* \equiv \frac{\nu_*}{\alpha} = \frac{\sigma \Gamma_\alpha \lambda_\alpha^2 n_H(z)}{4\pi^2 H^2(z)} \simeq \frac{\sigma \Gamma_\alpha \lambda_\alpha^2 n_H(0)}{4\pi^2 \Omega_m H_0^2} \simeq 6.72 \left( \frac{\Omega_b}{\Omega_m} \right) \text{ Mpc}. \quad (42)$$

Dimensionless frequency and radius variables are then given by  $\tilde{\nu} = (\nu_\alpha - \nu)/\nu_*$  and  $\tilde{r} = r/r_*$ . In these units, a photon emitted at frequency  $\tilde{\nu}_{\text{em}}$  will redshift over a distance  $\tilde{r}$  to  $\tilde{\nu}(\tilde{r}) = \tilde{\nu}_{\text{em}} + \tilde{r}$ . It is also useful to define a dimensionless radiation intensity  $\tilde{I} = I_\nu/I_\alpha^l$  or  $\tilde{J} = J_\nu/I_\alpha^l$ , where  $I_\alpha^l = \dot{N}_\alpha/(r_*^2 \nu_*)$ . Loeb & Rybicki derived an analytic solution for the mean intensity arising from a Ly $\alpha$  point source in the homogeneous expanding medium, applicable in the diffusion limit:

$$\tilde{J}(\tilde{r}, \tilde{\nu}) = \frac{1}{4\pi} \left( \frac{9}{4\pi \tilde{\nu}^3} \right)^{3/2} \exp\left(-\frac{9\tilde{r}^2}{4\tilde{\nu}^3}\right). \quad (43)$$

The corresponding scattering rate per atom is

$$P_\alpha \equiv 4\pi\sigma \int J_\nu(r) \varphi(\nu) d\nu = \sigma I_\alpha^l \tilde{P}_\alpha, \quad (44)$$

where the dimensionless scattering rate  $\tilde{P}_\alpha$  is given by

$$\tilde{P}_\alpha = \frac{1}{3\pi^{3/2}} \left( \frac{4}{9} \right)^{1/3} \Gamma\left(\frac{11}{6}\right) \gamma \tilde{r}^{-11/3}. \quad (45)$$

Here  $\gamma = H(z)/[\sigma \lambda_\alpha n_H(z)]$  is the Sobolev parameter for a uniform velocity gradient  $H(z)$ . The flux in the diffusion limit is straightforwardly derived from  $\tilde{J}$ :

$$\tilde{H}(\tilde{r}, \tilde{\nu}) = -\frac{1}{3\tilde{\chi}} \frac{\partial \tilde{J}}{\partial \tilde{r}} = \frac{3\tilde{r}}{8\pi \tilde{\nu}} \left( \frac{9}{4\pi \tilde{\nu}^3} \right)^{3/2} \exp\left(-\frac{9\tilde{r}^2}{4\tilde{\nu}^3}\right) \quad (46)$$

where  $\tilde{\chi} \equiv r_* \chi_\nu = \tilde{\nu}^{-2}$ . Details of the derivation are provided in Appendix C.

In this section, we attempt to reproduce the analytic solution using the moment equation solution method, before solving the problem more generally (outwith the diffusion limit) using the ray and moment equation methods and comparing with the Monte Carlo solution. We continue to assume coherent scattering. We take our grid in radius to be spaced logarithmically from  $\tilde{R}_C$  to  $\tilde{R}$ . Anticipating results comparable to those shown by Loeb & Rybicki, we adopt  $\tilde{R}_C = 10^{-3}$  and  $\tilde{R} = 10^2$ . The inner boundary condition for the moment equations is given by directly specifying the flux at the boundary according to equation (46), while in the ray equations we assume the same form for the flux with an angular dependence given by the diffusion limit as in equation (13). The outer boundary condition results from assuming no photons are scattered back into the system from  $\tilde{r} \geq \tilde{R}$ . This is technically not guaranteed to apply in an infinite scattering medium, but we expect no significant effect on the solution at distances well within the outer surface. Our frequency grid is subject to the restriction that the highest frequency (and therefore smallest value of  $\tilde{\nu}$ ) lies bluewards of any frequency at which there are photons, in order to ensure compatibility with the frequency initial condition equation (15). This may be ensured by taking  $\tilde{\nu}_1$  to lie blueward of the frequency of the least-redshifted photons emitted by the source as arises from free streaming, which requires that  $\tilde{\nu}_1 < \tilde{R}_C$ . We use a logarithmically spaced grid spanning the range from  $\tilde{\nu}_1 = 10^{-3.5}$  to  $\tilde{\nu}_{\text{NF}} = 10^{1.5}$ .

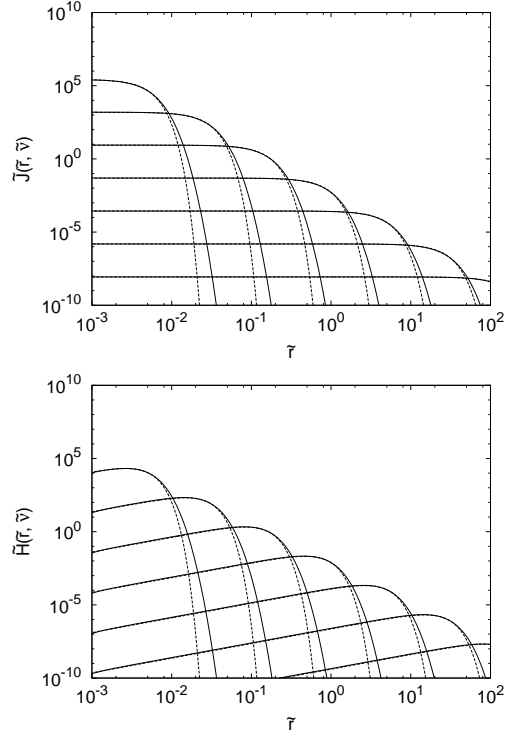


**Figure 3.** The mean intensity  $\tilde{J}(\tilde{r}, \tilde{\nu})$  (upper panel) and flux  $\tilde{H}(\tilde{r}, \tilde{\nu})$  (lower panel) for a point emission line source in a uniformly expanding homogeneous medium, from the moment equations in the diffusion approximation (solid lines) together with the analytic diffusion solutions (dashed lines). Coherent scattering is assumed. Profiles are given for  $\log_{10} \tilde{\nu} = -1.5, -1.0, -0.5, 0.0, 0.5, 1.0, 1.5$  in order of decreasing values of  $\tilde{J}$  or  $\tilde{H}$ .

A zero-temperature medium is assumed that provides no Doppler broadening of the Ly $\alpha$  line, giving a Lorentz profile for the opacity which in the wings takes the form  $\tilde{\chi} = 1/\tilde{\nu}^2$ . The frequency redistribution function results in coherent scattering, so that the source function is simply  $S_\nu(r) = J_\nu(r)$ . From equation (A4), the redistribution coefficients for coherent scattering simplify to  $\mathcal{R}_{k',k,d} \rightarrow \delta_{k',k}$ . When estimating the source function in order to solve the ray equations it is sufficient to take  $S_{k,d} = J_{k,d}$  and assume the analytic solution equation (43). The analytic expressions equations (43) and (46) apply in the diffusion approximation where the Eddington approximation is used, and the frequency derivative of the flux is assumed to be negligible. The former point requires  $f_\nu(r) \equiv 1/3$  (note that as the velocity law is linear,  $\beta \equiv 1$  and the equations are independent of  $g_\nu(r)$ ), while the latter is enforced explicitly by setting to zero corresponding elements in the matrices used to solve the problem (details are given in Higgins (2012)). The resulting solutions of the moment equations for  $\tilde{J}$  and  $\tilde{H}$  are given in Fig. 3. They agree very well with the analytic solutions, deviating only beyond the cutoff radius where the finiteness of the frequency grid restricts the solution from following the steep decline with radius.

A more comprehensive illustration of the utility of the combined ray and moment equation solution method is provided by seeking an exact solution to the homogeneous expanding medium problem and comparing our results with



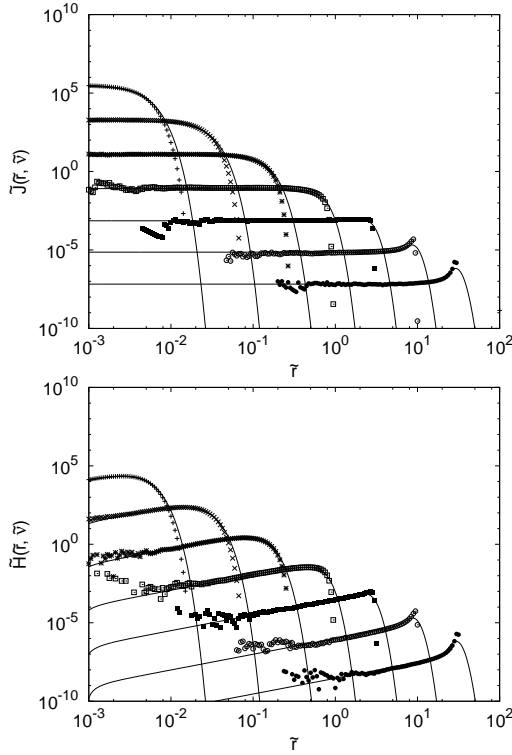


**Figure 4.** The mean intensity  $\tilde{J}(\tilde{r}, \tilde{\nu})$  (upper panel) and flux  $\tilde{H}(\tilde{r}, \tilde{\nu})$  (lower panel) for a point emission line source in a uniformly expanding homogeneous medium, obtained from two iterations of the combined ray/moment method with a diffusion solution inner boundary condition (solid lines), compared with the respective Monte Carlo solutions (various points). Coherent scattering is assumed. Profiles are given for  $\log_{10} \tilde{\nu} = -1.5, -1.0, -0.5, 0.0, 0.5, 1.0, 1.5$  in order of decreasing values of  $\tilde{J}$  or  $\tilde{H}$ .

the Monte Carlo solutions. We take as an inner boundary condition the analytic solution equation (46); this is physically reasonable as the moment equations are expected to converge to the diffusion limit at great optical depths. The corresponding Monte Carlo solution for the mean intensity  $\tilde{J}$  is obtained from the summed path-length method of Section 3, while the solution for the flux  $\tilde{H}$  is obtained from the definition of specific intensity and the appropriate angular integration. In Fig. 4 we compare the results of the combined ray/moment equation solution method and the Monte Carlo solution method. The Monte Carlo solutions are normalised by expressing the timescale  $\Delta t$  in equation (B7) and equation (B8) as  $\Delta t = N/\dot{N}_\alpha$ . The solutions are based on  $N = 10^7$  photon packets. Both the mean intensity and the flux obtained from the ray/moment method closely match the corresponding solutions determined from the Monte Carlo method. The cusps at large  $\tilde{r}$  for the higher values of  $\log_{10} \tilde{\nu}$  agree with those found by Loeb & Rybicki, who attributed them to causal limitation at the surface  $\tilde{r} = \tilde{\nu}$ . The solutions were obtained from two iterations: the moment solution, determined using Eddington factors from the ray solution, determines the source function estimate for a second ray solution, which determines the Eddington factors for a second moment solution. Upon further iterations we found that both methods had converged upon the same solution, independent of the initial estimate of the

source function used in the first ray solution, as we tested by using a free streaming source function estimate of the form  $\tilde{J} = \delta_D(\tilde{\nu} - \tilde{r})/(4\pi\tilde{r})^2$ . We also solved the problem using an inner free streaming boundary condition of the form  $\tilde{H} = \delta_D(\tilde{\nu} - \tilde{R}_C)/(4\pi\tilde{R}_C)^2$ . Except on the inner boundary, the solutions are identical to those produced by the diffusion boundary condition.

### 4.3 Homogeneous Expanding Medium: Analytic Results for a Continuum Source

We consider the problem of Ly $\alpha$  scattering about a continuum point source of UV photons in the neutral hydrogen intergalactic medium at high redshift, prior to the large-scale onset of reionisation. It is assumed that the scattering medium may be treated as spherically symmetric, at least in the vicinity of the source. The problem is then identical to that treated by Loeb & Rybicki (1999), with the exception of the frequency dependence of the source, which is here taken to be spectrally flat. The source term analogous to equation (40) is

$$S(\nu, r) = \dot{N}_\nu \frac{\delta(r)}{(4\pi r)^2} \quad (47)$$

where the constant  $\dot{N}_\nu$  is the rate of emission of photons per unit frequency. The parametrization of the radiative transfer equation proceeds identically to the case of a Ly $\alpha$  source, with the exception of the characteristic intensity which is defined as  $I_*^c = \dot{N}_\nu/r_*^2$ . It is useful to generalise the frequency dependence of the source by assuming a limiting frequency  $\nu_m$  bluewards of the resonance frequency beyond which no photons are emitted:

$$S(\nu, r) = \dot{N}_\nu \frac{\delta(r)}{(4\pi r)^2} \times \Theta(\nu_m - \nu) \quad (48)$$

where the step function  $\Theta(\nu_m - \nu)$  is equal to unity for  $\nu < \nu_m$  (or equivalently  $\tilde{\nu} > \tilde{\nu}_m$ ) and is zero otherwise. We show in Appendix C that the resulting radiation field in the diffusion limit is described by the solutions

$$\begin{aligned} \tilde{J}(\tilde{r}, \tilde{\nu}) &= \left(\frac{16}{3}\right)^{1/3} \frac{2}{(4\pi)^{5/2}} \frac{1}{\tilde{r}^{7/3}} \\ &\times \int_{\frac{9\tilde{r}^2}{4(\tilde{\nu}^3 - \tilde{\nu}_m^3)}}^{\infty} du \left(t + \frac{1}{u}\right)^{-2/3} u^{-1/2} e^{-u}, \end{aligned} \quad (49)$$

$$\begin{aligned} \tilde{H}(\tilde{r}, \tilde{\nu}) &= \left(\frac{4^5}{3^4}\right)^{1/3} \frac{1}{(4\pi)^{5/2}} \frac{\tilde{\nu}^2}{\tilde{r}^{10/3}} \\ &\times \int_{\frac{9\tilde{r}^2}{4(\tilde{\nu}^3 - \tilde{\nu}_m^3)}}^{\infty} du \left(t + \frac{1}{u}\right)^{-2/3} u^{1/2} e^{-u}, \end{aligned} \quad (50)$$

where  $t = -4\tilde{\nu}^3/9\tilde{r}^2$ . Note that in the case of a spectrally flat source with no blue cutoff frequency,  $\tilde{\nu}_m \rightarrow -\infty$  and the lower limit in each integral reduces to zero.

The solutions are shown as a series of frequency profiles in Fig. 5. (Some small numerical artefacts resulting from the numerical integration have been interpolated over for the purpose of presentation.) We find a peak in both the mean intensity and the flux that drifts redwards further from the source, corresponding to the contribution from photons emitted by the source at the line centre. This is seen from

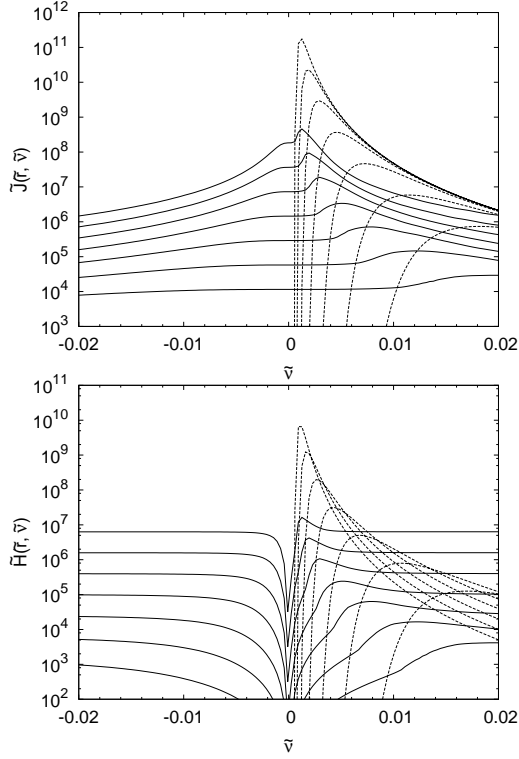


**Figure 5.** Analytic solution for  $\tilde{J}$  (upper panel) and  $\tilde{H}$  (lower panel) for a spectrally flat source in a uniformly expanding homogeneous medium in the zero-temperature diffusion approximation (solid lines), together with the corresponding analytic solution of Loeb & Rybicki for a monochromatic Ly $\alpha$  source (dashed lines). Values of  $\tilde{r}$  are given by  $10^{-4.5}$ ,  $10^{-4.2}$ ,  $10^{-3.9}$ ,  $10^{-3.6}$ ,  $10^{-3.3}$ ,  $10^{-3.0}$ ,  $10^{-2.7}$  in order of decreasing  $\tilde{J}$  or  $\tilde{H}$ .

a comparison of the peak frequency with that found from the analytic solutions for  $\tilde{J}$  and  $\tilde{H}$  for a monochromatic Ly $\alpha$  source, given by equations (43) and (46). By solving  $\partial\tilde{J}/\partial\tilde{\nu} = 0$  for the analytic solution of Loeb & Rybicki, we find the frequency of the peak satisfies  $\tilde{\nu} = (3/2)^{1/3}\tilde{r}^{2/3}$ .

The most physically relevant aspect of the Ly $\alpha$  solution to the 21cm signature is the Ly $\alpha$  scattering rate. As shown in the upper panel of Fig. 5,  $\tilde{J}(x)$  is approximately flat across the line centre at radii exceeding some minimum distance from the source. The scattering rate then varies as the average intensity at line centre,

$$P_\alpha \equiv 4\pi\sigma \int J_\nu(r)\varphi(\nu) d\nu \simeq 4\pi\sigma I_*^c \tilde{J}(\tilde{r}, 0) \quad (51)$$

where

$$\begin{aligned} \tilde{J}(\tilde{r}, 0) &= \frac{2^{7/3}}{3^{1/3}(4\pi)^{5/2}\tilde{r}^{7/3}} \int_{\frac{9\tilde{r}^2}{4|\tilde{\nu}_m|^3}}^{\infty} t^{1/6} e^{-t} dt \\ &= \frac{2^{7/3}}{3^{1/3}(4\pi)^{5/2}\tilde{r}^{7/3}} \times \Gamma\left(\frac{7}{6}, \frac{9\tilde{r}^2}{4|\tilde{\nu}_m|^3}\right), \end{aligned} \quad (52)$$

and  $\Gamma(q, y) \equiv \int_y^\infty u^{q-1} e^{-u} du$  is the upper incomplete Gamma function. The solution saturates with  $\Gamma(7/6, y) \rightarrow \Gamma(7/6) \simeq 0.93$  for values of the argument  $y \lesssim 10^{-2}$  or, for our problem,  $\tilde{r} \lesssim 0.1 \times (2/3)|\tilde{\nu}_m|^{3/2}$ . In this limit, the dimensionless scattering rate  $\tilde{P}_\alpha = P_\alpha/(\sigma I_*^c)$  becomes

$$\tilde{P}_\alpha^{\text{diff}} \equiv \frac{2^{7/3}\Gamma(7/6)}{3^{1/3}(4\pi)^{3/2}\tilde{r}^{7/3}}. \quad (53)$$

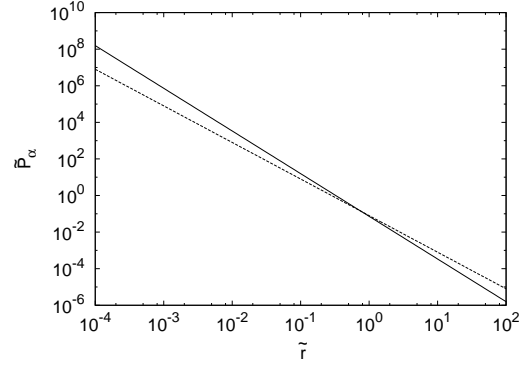


**Figure 6.** Scaled scattering rate for diffusion solution with flat spectrum extending infinitely bluewards,  $\tilde{P}_\alpha^{\text{diff}}$  (solid line) and expected result in the corresponding free-streaming limit,  $\tilde{P}_\alpha^{\text{free}}$  (dashed line).

This form for the scattering rate applies for all  $\tilde{r}$  if  $|\nu_m| \rightarrow \infty$  and thus applies in the absence of any cutoff in the source spectrum. For a finite  $|\nu_m|$  the effect of the cutoff is to suppress  $\tilde{J}(\tilde{r}, 0)$  for sufficiently large  $\tilde{r}$ : physically this corresponds to the redshifting past line centre of all photons at these radii.

A useful comparison may be made with the expected scattering rate in the free streaming limit. The solution is  $\tilde{J} = \Theta(\tilde{\nu} - \tilde{\nu}_m - \tilde{r})/(4\pi\tilde{r})^2$  and the corresponding scattering rate for sufficiently negative  $\tilde{\nu}_m$  is simply

$$\tilde{P}_\alpha^{\text{free}} \equiv \frac{1}{4\pi\tilde{r}^2}. \quad (54)$$

We show the radial dependence of the Ly $\alpha$  scattering rate induced around the source in Fig. 6. The diffusion limit scattering rate exceeds the corresponding result in the free-streaming limit close to the source and decreases to below the free-streaming rate at  $\tilde{r} \geq 2^7(\Gamma(7/6))^3/(3(4\pi)^{3/2}) \simeq 0.75$ .

The size of the Ly $\alpha$  scattering region around the source is given by the maximum radius at which the scattering rate is non-zero. This radius will depend upon  $\tilde{\nu}_m$ , which we take to be the bluest frequency at which the source emits photons that are capable of redshifting into the Ly $\alpha$  line. Typically this cutoff will be the Ly $\beta$  frequency,  $\nu_\beta = (32/27)\nu_\alpha$ , as photons emitted bluewards of Ly $\beta$  will redshift into the Ly $\beta$  or higher-energy resonance lines and do not produce Ly $\alpha$  photons (except as products of radiative cascades which we do not consider here). Assuming a Ly $\alpha$  source term of the form of equation (48), the scattering rate found in the diffusion limit given by equation (52) is found to decrease below one-tenth of its value in the absence of a cutoff when the second argument  $y$  of the upper incomplete Gamma function satisfies  $y \geq f \simeq 2.5$ , or

$$\tilde{r} \geq (2/3)f^{1/2}|\tilde{\nu}_\beta|^{3/2} \simeq 1.05|\tilde{\nu}_\beta|^{3/2}. \quad (55)$$

Outside of the diffusion regime, an upper limit for the size of the Ly $\alpha$  scattering region is given by free streaming: all photons will have redshifted past the line centre at radii  $\tilde{r} > |\tilde{\nu}_\beta|$ .

The number of scatters a Ly $\alpha$  photon undergoes before escaping the IGM may be computed as the ratio of the total rate of scatters through a region of radius  $r_{\text{max}}$  and the

emission rate:

$$\begin{aligned}
 N_{\text{scatt}} &= \dot{N}_\alpha^{-1} 4\pi \int_0^{r_{\text{max}}} dr r^2 n_{\text{H}}(z) P_\alpha(r) \\
 &\simeq \left[ \frac{12^{2/3}}{(4\pi)^{1/2}} \Gamma\left(\frac{7}{6}\right) \tilde{r}_{\text{hor}}^{-1} - \tilde{r}_{\text{hor}}^{-1} + \frac{\tilde{r}_{\text{max}}}{\tilde{r}_{\text{hor}}} \right] \gamma^{-1} \\
 &\simeq \gamma^{-1} \frac{\tilde{r}_{\text{max}}}{\tilde{r}_{\text{hor}}}, \quad (56)
 \end{aligned}$$

where equation (53) is used for  $0 < \tilde{r} < 1$  and equation (54) for  $\tilde{r} > 1$ . Here  $r_{\text{hor}} = (5/27)c/H(z)$  is the ‘horizon’ distance a photon emitted just longward of the Ly $\beta$  resonance frequency may travel before redshifting into the local Ly $\alpha$  resonance frequency, and the total Ly $\alpha$  photon production rate is taken as  $\dot{N}_\alpha = \dot{N}_\nu(\nu_\beta - \nu_\alpha) = (5/27)\dot{N}_\nu\nu_\alpha$ .

For the Wouthuysen-Field effect to compete with the CMB and couple the spin temperature to the gas kinetic temperature, a critical thermalization Ly $\alpha$  scattering rate of  $P_{\text{th}} = 27A_{10}T_{\text{CMB}}/4T_*$  is required, where  $A_{10} \simeq 2.85 \times 10^{-15} \text{ s}^{-1}$  is the 21-cm transition rate,  $T_* \equiv h\nu_{10}/k_B \simeq 0.068 \text{ K}$  and  $T_{\text{CMB}}$  is the temperature of the Cosmic Microwave Background (Madau et al. 1997). For a continuum source, from equations (51) and (53) the critical thermalization photon production rate between the Ly $\alpha$  and Ly $\beta$  resonance line frequencies is

$$\dot{N}_{\alpha,\text{th}}^{\text{cont}} \simeq 4.39 \times 10^{55} \left( \frac{1+z}{11} \right) r_{\text{Mpc}}^{7/3} \text{ s}^{-1} \quad (57)$$

where  $r_{\text{Mpc}}$  is the distance from the source in megaparsecs. Here we adopted properties corresponding to the mean intergalactic medium at  $z = 10$ , taking the baryon and dark matter density parameters  $\Omega_b h^2 = 0.022$  and  $\Omega_m = 0.27$ , respectively, and Hubble constant  $H_0 = 70 \text{ km s}^{-1} \text{ Mpc}^{-1}$ , consistent with the results of Komatsu et al. (2011). These values give  $\nu_* = 1.25 \times 10^{13} [(1+z)/11]^{3/2} \text{ Hz}$  and  $r_* = 1.12 \text{ Mpc}$  (independent of redshift). The Sobolev parameter is  $\gamma = \nu_\alpha H/(\sigma c n_{\text{H}}) \simeq 1.27 \times 10^{-6} [(1+z)/11]^{-3/2}$ . Thus a source with a continuum luminosity of  $\sim 2 \times 10^{11} L_\odot$  would be able to couple the spin temperature to the gas kinetic temperature out to a distance of 1 Mpc. This is far less demanding than for an emission-line source. From equations (44) and (45), the required Ly $\alpha$  photon production rate is

$$\dot{N}_{\alpha,\text{th}}^{\text{line}} \simeq 1.38 \times 10^{60} \left( \frac{1+z}{11} \right)^4 r_{\text{Mpc}}^{11/3} \text{ s}^{-1}. \quad (58)$$

An emission-line source with a Ly $\alpha$  luminosity as great as  $10^{12} L_\odot$  would be able to couple the spin temperature to the gas temperature only out to a distance of  $\sim 90 \text{ kpc}$ . Indeed, at this distance, if the source were a radio-loud AGN, its radio emission would likely dominate the coupling of the spin temperature (Madau et al. 1997).

#### 4.4 Homogeneous Expanding Medium: Numerical Results for a Continuum Source

Outside of the zero-temperature regime treated by Loeb & Rybicki for a monochromatic source, it is necessary to specify the physical state of the scattering medium. We adopt properties corresponding to the mean intergalactic medium at  $z = 10$  as above, with an assumed gas temperature  $T = 10 \text{ K}$ .

In solving the moment equations, the initial condition in

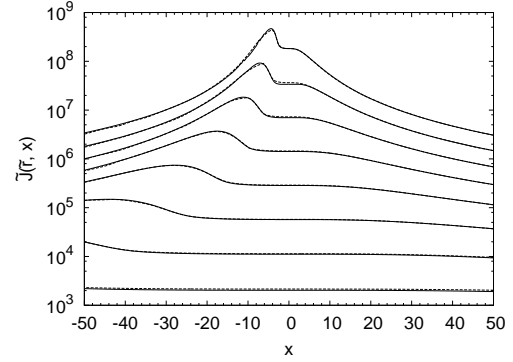


**Figure 7.** Diffusion approximation moment solution for  $\tilde{J}$  in a uniformly expanding homogeneous medium assuming coherent scattering and a Voigt line profile (solid line), together with the corresponding analytic solution in the wing approximation (dashed line). The frequency dependence is shown as a function of  $x$  assuming a temperature  $T = 10 \text{ K}$  for values of  $\tilde{r}$  given by  $10^{-4.5}$ ,  $10^{-4.2}$ ,  $10^{-3.9}$ ,  $10^{-3.6}$ ,  $10^{-3.3}$ ,  $10^{-3.0}$ ,  $10^{-2.7}$ ,  $10^{-2.4}$ .

frequency is enforced by taking our frequency grid to start from  $\tilde{\nu}_1 < \tilde{\nu}_m$ , i.e. the frequency grid must extend bluewards of the source emission cutoff frequency. Unless otherwise stated, we have taken  $x_m = -(\nu_*/\Delta\nu_D)\tilde{\nu}_m = 1000$  for all solutions. We use two frequency grids, one with a small frequency spacing across the line centre for  $x$  lying in the range  $[-x_{\text{max}}, x_{\text{max}}]$  where  $x_{\text{max}} = 60$  (unless stated otherwise), and a second grid with a larger frequency spacing across  $[x_{\text{max}}, x_1]$ . We adopt the analytic solutions to satisfy the inner and outer boundary conditions for the moment equations in the diffusion approximation. We solve the moment equations with the addition of the full Voigt profile form for  $\chi_\nu$  with an opacity given by  $\tilde{\chi} = \sqrt{\pi} r_* \kappa_0 \phi_V(x)$ . The diffusion limit is enforced by setting  $f_\nu(r) = 1/3$ , and the appropriate matrix elements representing the frequency derivative of the flux in the solution method are set to zero to match the diffusion equation. Our moment solution for  $\tilde{J}$  is shown in Fig. 7. It nearly coincides with the analytic solution, demonstrating that the assumption of the wing form of the opacity does not affect the solution in this approximation. A similarly identical solution was found for the flux. As a consequence, the solutions as a function of frequency are very insensitive to the temperature of the medium in the coherent scattering approximation.

We solved the problem using the ray/moment method applied to the exact forms of the ray and moment equations for the uniformly expanding homogeneous medium problem. Again, we used the Voigt profile form for  $\tilde{\chi}$  and assumed coherent scattering. We assumed the diffusion limit solutions given by equations (49) and (50) in specifying the inner boundary condition and the initial estimate of the source function used in solving the ray equations. Note that for this and subsequent problems where the conditions do not match those that determine the solution used for the boundary condition, the ray/moment solution at the boundary is subject to an unphysical constraint and we should not assume it is accurate on the boundary.

Our ray/moment solution is displayed in Fig. 8. For distances sufficiently far from the source we find the ray/moment solution is a close match to the diffusion ap-

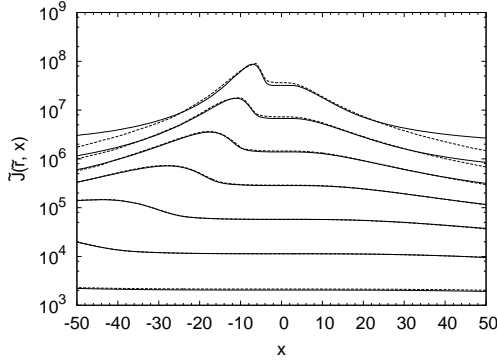


**Figure 8.** Coherent scattering solution for  $\tilde{J}$  obtained from ray and moment equations (solid lines), compared with the analytic solutions in the zero-temperature diffusion approximation (dashed lines). Frequency profiles correspond to radii  $\tilde{r} = 10^{-4.2}, 10^{-3.9}, 10^{-3.6}, 10^{-3.3}, 10^{-3.0}, 10^{-2.7}, 10^{-2.4}$ .

proximation solution. Closer to the source we find both solutions match reasonably well across the line centre, while away from line centre there is some deviation. The ray/moment solution approaches a flat profile closer to the free-streaming solution. This is an expected consequence of the negligible optical depth out to these radii away from line centre. We have checked the Eddington factor and found  $f_\nu \simeq 1/3$  except in the wings, with the deviation from  $1/3$  matching the deviation in the wings between the two solutions shown in Fig. 8. We found that the flux is altered from the analytic solution to a similarly limited extent.

The accuracy of the solutions may be checked by use of an integral constraint on the number of photons obtained from the radiative transfer equation. It may be derived from the zeroth-order moment equation obtained from equation (C1) with  $V = Hr$  and  $\delta(\tilde{\nu}) \rightarrow 1$  for a continuum source in a homogeneous expanding medium by multiplying it by  $\tilde{r}^2$ , integrating in radius from  $\tilde{r} = 0$  to  $\tilde{R}$  and in frequency across the line centre from  $-\tilde{\nu}_{\max}$  to  $+\tilde{\nu}_{\max}$ , causing the terms corresponding to the opacity and emissivity to cancel out due to radiative equilibrium. The result is

$$\int_0^{\tilde{R}} \tilde{r}^2 \left[ \tilde{J}(\tilde{r}, \tilde{\nu}_{\max}) - \tilde{J}(\tilde{r}, -\tilde{\nu}_{\max}) \right] d\tilde{r} + \tilde{R}^2 \int_{-\tilde{\nu}_{\max}}^{\tilde{\nu}_{\max}} \tilde{H}(\tilde{R}, \tilde{\nu}) d\tilde{\nu} = \frac{2\tilde{\nu}_{\max}}{(4\pi)^2}. \quad (59)$$

We have verified that all the solutions examined in this section satisfy this constraint.

The assumption of coherent scattering is valid for photons scattering at frequencies far from line centre, but as we examine photons redshifting across the line centre such an assumption is not physically motivated. We now treat the added effect of Doppler shifts due to the thermal- and recoil-induced atomic velocities. The thermal velocities of the atoms are responsible for the RII frequency redistribution function for Ly $\alpha$  scattering. For convergence with recoils, we found it necessary to increase  $x_{\max}$  to 200. We first consider the addition of RII redistribution in isolation by ignoring the effect of recoils. Ray/moment equation solutions are obtained similarly to the coherent solution with the RII form for the coefficients  $\mathcal{R}_{k',k,d}$  with  $\epsilon = 0$  as given in equa-

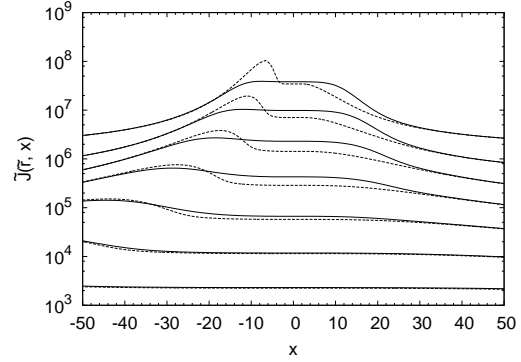


**Figure 9.** RII redistribution solution for  $\tilde{J}$  obtained from ray and moment equations (solid lines), compared with the corresponding solution for coherent scattering (dashed lines). Frequency profiles correspond to radii  $\tilde{r} = 10^{-4.2}, 10^{-3.9}, 10^{-3.6}, 10^{-3.3}, 10^{-3.0}, 10^{-2.7}, 10^{-2.4}$ .

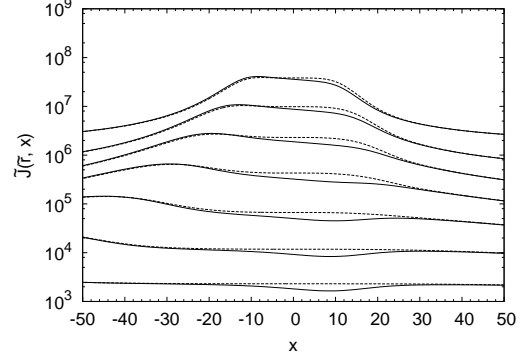


**Figure 10.** RII redistribution solution with recoil obtained from ray and moment equations (solid lines), compared with the corresponding solution for RII redistribution without recoil (dashed lines). Frequency profiles correspond to radii  $\tilde{r} = 10^{-4.2}, 10^{-3.9}, 10^{-3.6}, 10^{-3.3}, 10^{-3.0}, 10^{-2.7}, 10^{-2.4}$ .

tion (A6) in Appendix A. We display our solution for  $\tilde{J}$  in Fig. 9. There is some redistribution of photons across the line centre relative to the red peak found in the coherent scattering case, resulting in a small boost in the mean intensity across the line centre over a limited range in radii. The difference in the spectrum from the coherent scattering case is not particularly significant at large radii.

We add the effect of atomic recoil by seeking ray/moment solutions without setting the recoil parameter  $\epsilon$  to zero. The resulting solution is displayed in Fig. 10. The expected Boltzmann distribution gradient is recovered across the line centre.

We also apply the Monte Carlo method described in Section 3 and Appendix B to the problem. We assume a continuum source that emits  $\dot{N}_\nu$  photons per second per Hz across the frequency range  $[x_{\min}, x_{\max}]$  where  $\dot{N}_\nu$  is independent of  $\nu$ ,

$$\dot{N}_\nu \Delta\nu = \frac{N}{\Delta t} \times \left( \frac{\Delta x}{x_{\max} - x_{\min}} \right) \quad (60)$$

where  $\Delta\nu$  is the frequency bin width and the factor in brackets is the fraction of the  $N$  photons emitted within a single

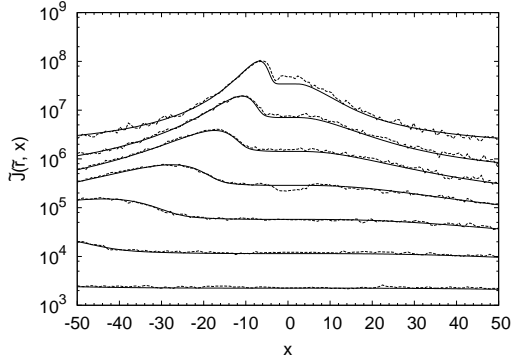


**Figure 11.** Monte Carlo solution (dashed lines) for coherent scattering, together with the corresponding ray/moment equation solution (solid lines). Frequency profiles correspond to radii  $\tilde{r} = 10^{-4.2}, 10^{-3.9}, 10^{-3.6}, 10^{-3.3}, 10^{-3.0}, 10^{-2.7}, 10^{-2.4}$ .

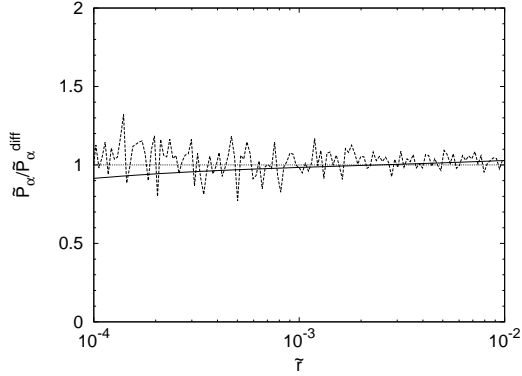


**Figure 12.** Scattering rates derived from numerical integration of ray/moment equation method (solid line) and Monte Carlo solution (long-dashed line), both for coherent scattering; normalised by the analytic result in the diffusion limit.

frequency bin. In the case of a source cutoff at  $x_m$ , we take  $x_{\max} = x_m$ . The solution is normalized by using  $\Delta t$  from equation (60) in equation (B7). The resulting dependence on the source strength  $\tilde{N}_\nu$  is scaled out when expressing the solution in terms of  $\tilde{J}$ . We obtained a solution for coherent scattering using  $N = 2 \times 10^5$  photon packets. The solution is displayed in Fig. 11. It closely matches the ray/moment solution. The corresponding scattering rate is shown in Fig. 12. It closely resembles the ray/moment solution scattering rate, which itself is nearly coincident over this range in radius with the diffusion approximation power law of equation (53). The noise level of the Monte Carlo solution is a few to several percent per radial bin, decreasing with increasing radius. Two hundred logarithmically spaced radial bins were used to cover the range  $-4.5 < \log_{10} \tilde{r} < -1.5$ .

We have determined the scattering rate profile from the ray/moment solution. Fig. 13 shows two examples with different values of the source upper frequency cutoff  $\nu_m$ . The upper panel has  $x_m = 100$  and thus  $|\tilde{\nu}_m| \simeq 10^{-1.6}$ . The ‘diffusion-limited’ effective radius of the Ly $\alpha$  scattering region, as given by equation (55) for general  $\tilde{\nu}_m$ , is  $\tilde{r} = 1.05|\tilde{\nu}_m|^{3/2} \simeq 10^{-2.3}$ , in approximate agreement with the figure.

The lower panel has  $x_m = x_\beta$ , where  $x_\beta =$

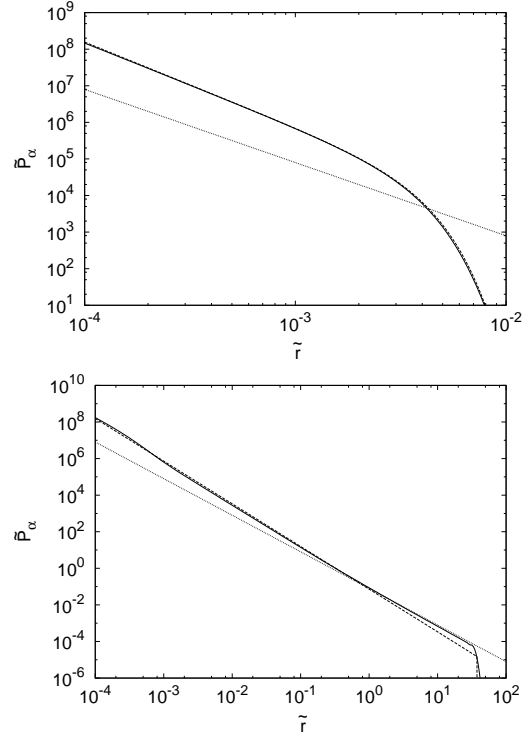


**Figure 13.** Scaled scattering rate for the IGM at  $z = 10$  with an assumed temperature  $T = 10$  K, derived from numerical integration of the scattering solution obtained from the ray/moment equations (solid line) and the analytic diffusion solution (dashed line, nearly coincident with the solid line in the upper panel), for source cutoff frequency  $x_m = 100$  and coherent scattering (upper panel) and  $x_m = 1.4 \times 10^5$  including RII redistribution and recoil (lower panel). For comparison we also show  $\tilde{P}_\alpha^{\text{free}}$  (dotted line).

$5\nu_\alpha/(27\Delta\nu_D) \simeq 1.4 \times 10^5$  denotes the source cutoff corresponding to the Ly $\beta$  frequency. This corresponds to  $-\tilde{\nu}_m \simeq 10^{1.6}$ . Photons with larger values of  $-\tilde{\nu}$  would not be able to redshift into the Ly $\alpha$  resonance at any greater distance, as they would encounter the Ly $\beta$  or a higher order Lyman resonance en route. The limiting distance the Ly $\alpha$  photons may travel is  $\tilde{r}_{\text{hor}} \simeq 38[(1+z)/11]^{-3/2}$  (the Ly $\alpha$  horizon). For  $\tilde{r} \lesssim 1$ , the diffusion limit applies and the scattering rate takes on the approximate  $\tilde{r}^{-7/3}$  scaling expected. At very small values,  $\tilde{r} \lesssim 10^{-3}$ , frequency redistribution substantially modifies the scattering rate, as shown in Fig. 14. As discussed in Appendix C, the diffusion approximation breaks down at  $\tilde{r} \gtrsim 1$  and the scattering rate takes on a profile closer to the free-streaming value  $1/4\pi\tilde{r}^2$ , as found in the Monte Carlo computations of Semelin et al. (2007). The scattering rate becomes vanishingly small at  $\tilde{r} > 29$ , as shown in Fig. 13. This is slightly shorter than the Ly $\alpha$  horizon distance by the factor 0.77 and appears to be a consequence of the causal limitation of the radiation field (see Loeb & Rybicki 1999).

The  $1/r^2$  behaviour of the mean intensity at large distances has an interesting implication for the global radiation field produced by a uniform distribution of sources of spatial number density  $n_0$ . The total scattering rate is limited by

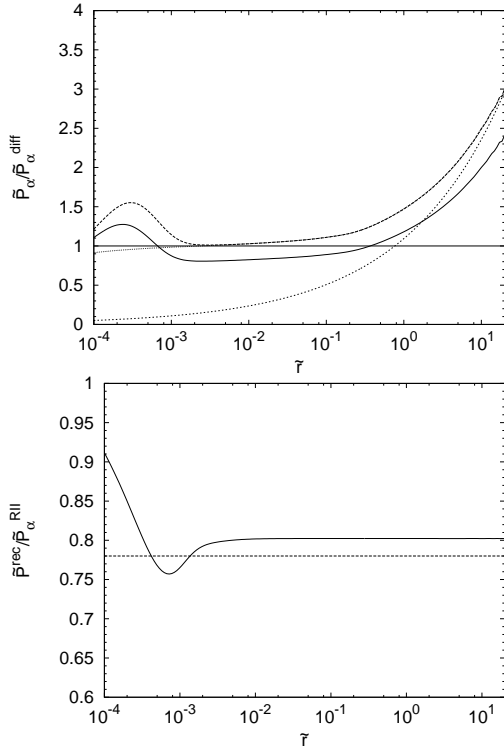


**Figure 14.** Upper panel: Ratio of scattering rate derived from numerical integration of the appropriate ray/moment solution, to the analytic diffusion limit result  $\tilde{P}_\alpha^{\text{diff}}$ , for RII redistribution with recoil (solid line), RII redistribution without recoil (dashed line) and coherent scattering without recoil, which coincides with the RII redistribution without recoil solution for  $\tilde{r} > 10^{-2.5}$  (dotted line). Also shown is the free-streaming result (short-dashed line). All solutions assume  $T = 10$  K and  $x_m = 1.4 \times 10^5$ . Lower panel: Ratio of scattering rate assuming RII redistribution with recoil to that assuming RII redistribution alone (solid line), compared with the estimate  $S_\alpha = 0.78$  (dashed line) of the suppression factor in a uniformly expanding homogeneous medium for a uniform radiation field (Furlanetto & Pritchard 2006).

the maximum distance  $\tilde{r}_{\text{max}}$  the Ly $\alpha$  photons travel:

$$\tilde{P}_\alpha^{\text{tot}} = 4\pi(n_0 r_*^3) \int_0^{\tilde{r}_{\text{max}}} d\tilde{r} \tilde{r}^2 \frac{1}{4\pi\tilde{r}^2} \simeq (n_0 r_*^3) \tilde{r}_{\text{max}}. \quad (61)$$

The maximum distance is given by the causal limitation radius  $\tilde{r}_{\text{max}} = \tilde{r}_{\text{causal}} \simeq 29 \lesssim \tilde{r}_{\text{hor}}$ . Given that the scattering rate at large distances somewhat exceeds  $1/4\pi\tilde{r}^2$  within the horizon, however, taking the maximum radius to be the horizon radius gives a very good approximation to the total scattering rate, and corresponds to  $N_{\text{scatt}} \simeq \gamma^{-1}$ .

It is instructive to compare this result with the estimate of Field (1959a), who expressed the scattering rate as the product of the production rate of Ly $\alpha$  photons per neutral hydrogen atom and the number of scatters  $N_{\text{scatt}}$  a photon undergoes before it redshifts sufficiently far from line centre to escape:  $P_\alpha = (n_0 \dot{N}_\alpha / n_H) N_{\text{scatt}}$ . He argued that for uniformly distributed sources in a homogeneous and isotropic medium,  $N_{\text{scatt}} = \gamma^{-1}$  (cf. Higgins & Meiksin 2009). Allowing for all photons emitted between the Ly $\alpha$  and Ly $\beta$  frequency resonances, this corresponds to the dimensionless scattering rate  $\tilde{P}_\alpha^{\text{Field}} = (n_0 r_*^3) \tilde{r}_{\text{hor}}$ . For a uniform radiation field, the total scattering rate is thus again given

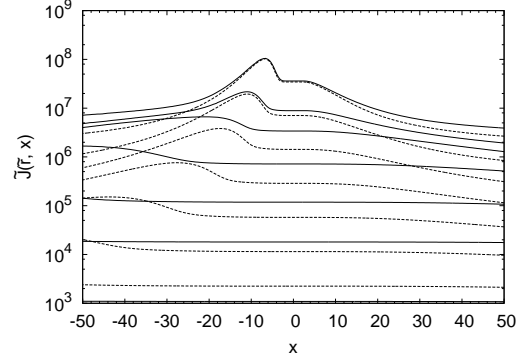


**Figure 15.** Coherent scattering solution obtained from ray and moment equations for the overdense shell given by equation (62) (solid lines), compared with the corresponding solution for a uniform density  $n_H(z)$  (dashed lines). Frequency profiles correspond to radii  $\tilde{r} = 10^{-4.2}, 10^{-3.9}, 10^{-3.6}, 10^{-3.3}, 10^{-3.0}, 10^{-2.7}, 10^{-2.4}$ .

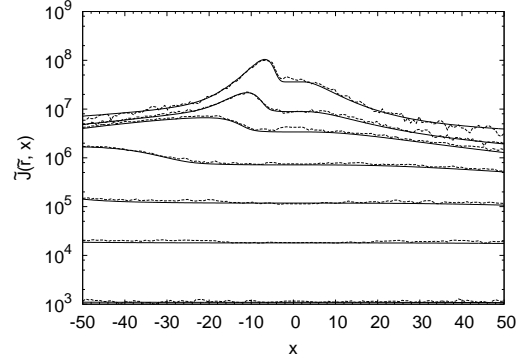


**Figure 16.** Monte Carlo solution (dashed lines) for coherent scattering with the density profile specified in equation (62), compared with the corresponding ray/moment equation solution (solid lines). Frequency profiles correspond to radii  $\tilde{r} = 10^{-4.2}, 10^{-3.9}, 10^{-3.6}, 10^{-3.3}, 10^{-3.0}, 10^{-2.7}, 10^{-2.4}$ .

by equation (61), with the maximum radius taking on the natural value  $\tilde{r}_{\text{max}} = \tilde{r}_{\text{hor}}$ .

Allowing for recoils suppresses the scattering rate relative to the RII case without recoil, as shown in the lower panel of Fig. 14. The suppression factor  $S_\alpha$  computed in the diffusion approximation by Furlanetto & Pritchard (2006) for an isotropic and homogeneous distribution of uniform sources in a uniformly expanding homogeneous medium is given by  $S_\alpha \simeq 0.78$ . This is close to the average value of the radius-dependent suppression factor determined from our solutions outwith the diffusion approximation.

## 5 APPLICATIONS TO INHOMOGENEOUS MEDIA

### 5.1 Overdense Shell

As an example application for an inhomogeneous density profile, we examine the continuum source Ly $\alpha$  scattering problem for a scattering medium undergoing Hubble expansion but including an overdense shell between  $10^{-3.5} < \tilde{r} <$

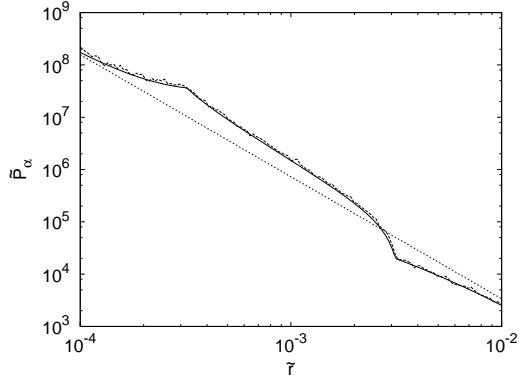


**Figure 17.** Scaled scattering rate derived from numerical integration of ray/moment equation solution (solid line) and Monte Carlo solution (long-dashed line) for coherent scattering in a medium with an overdense shell given by equation (62). For comparison we also show  $\tilde{\mu}_\alpha^{\text{diff}}$  (short-dashed line).

$10^{-2.5}$ ;

$$n_H(r) = \begin{cases} 10 \times n_H(z) & ; \quad 10^{-3.5} \leq \tilde{r} \leq 10^{-2.5} \\ n_H(z) & ; \quad \tilde{r} < 10^{-3.5}, \tilde{r} > 10^{-2.5} \end{cases} \quad (62)$$

The IGM temperature is  $T = 10$  K. This affects the spatial dependence of the opacity coefficients  $\chi_{k,d}$  for the ray/moment equations method. We show the ray/moment solution to the problem for coherent scattering in Fig. 15, while the corresponding scattering rate is denoted by the solid line in Fig. 17. Compared with the spectrum for a uniform density scattering medium, the frequency peaks at the overdense radii are displaced further redward, while the scattering rate across this range is boosted. At the outer edge of the shell the scattering rate dips below the uniform density value.

The corresponding Monte Carlo solution to the problem is shown in Fig. 16. ( $N = 2 \times 10^5$  photon packets were used.) Significantly more time was required to follow the photon packets through the overdensity compared with the homogeneous density case. The corresponding scattering rate is displayed in Fig. 17.

## 5.2 Quadratic Velocity Profile

In this section we consider a continuum source in a medium of uniform density, however we move beyond the assumption of a simple Hubble velocity profile  $V = Hr$ . To examine the specific effects of a non-linear velocity profile alone, we consider the case of a quadratic velocity law. We parametrize the radial velocity profile  $V(r)$  for  $R_{\min} < r < R_{\max}$  by

$$V(r) = (V_{\max} - V_{\min}) \left( \frac{r - R_{\min}}{R_{\max} - R_{\min}} \right)^2 + V_{\min}. \quad (63)$$

We show both the quadratic velocity profile given by equation (63) and the corresponding Hubble profile in Fig. 18, where we have taken  $V_{\max} \equiv V(R_{\max}) = HR_{\max}$  and  $V_{\min} \equiv V(R_{\min}) = HR_{\min}$ . Using this velocity profile we obtain Ly $\alpha$  radiative transfer solutions from the ray/moment method. The IGM temperature is  $T = 10$  K. The solution assuming coherent scattering is displayed in Fig. 19. In order to isolate the effect of the velocity profile, the solution is compared with the equivalent ray/moment solution for Hubble

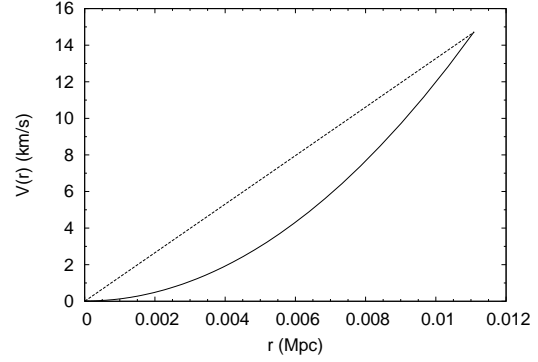


**Figure 18.** Velocity profile given by the quadratic relation of equation (63) with  $\tilde{R}_{\min} = 10^{-5}$ ,  $\tilde{R}_{\max} = 10^{-2}$  and  $V_{\max/\min} = HR_{\max/\min}$  (solid line), compared with the Hubble law  $V(r) = Hr$  (dashed line).

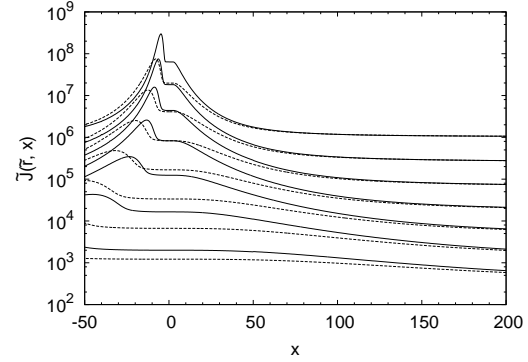


**Figure 19.** Coherent scattering solution obtained from ray and moment equations with the quadratic velocity profile of equation (63) (solid lines), compared with the corresponding solution for a Hubble velocity profile (dashed lines). Frequency profiles correspond to radii  $\tilde{r} = 10^{-4.1}, 10^{-3.8}, 10^{-3.5}, 10^{-3.2}, 10^{-2.9}, 10^{-2.6}, 10^{-2.3}$ .

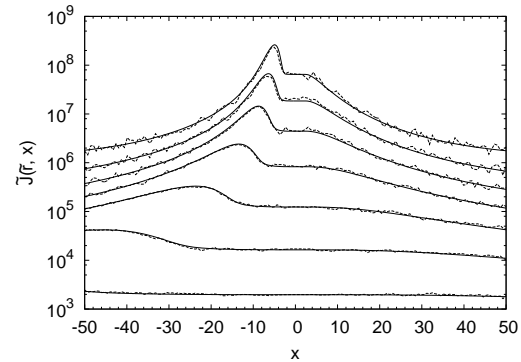


**Figure 20.** Monte Carlo solution (dashed lines) for coherent scattering with the quadratic velocity profile of equation (63), compared with the corresponding ray/moment equation solution (solid line). Frequency profiles correspond to radii  $\tilde{r} = 10^{-4.1}, 10^{-3.8}, 10^{-3.5}, 10^{-3.2}, 10^{-2.9}, 10^{-2.6}, 10^{-2.3}$ .

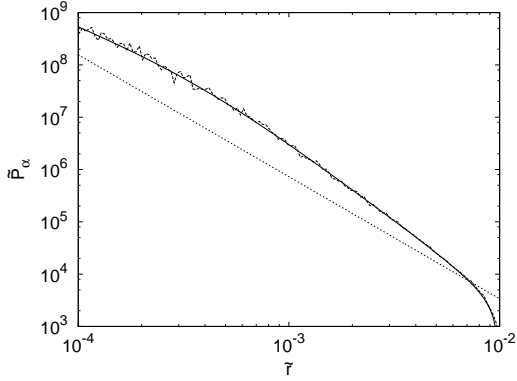


**Figure 21.** Scaled scattering rate for a uniform medium with a velocity profile given by equation (63), derived from numerical integration of the ray/moment equation method (solid line) for coherent scattering, together with the corresponding scattering rate obtained from the Monte Carlo method (long-dashed line). For comparison we also show  $\tilde{P}_\alpha^{\text{diff}}$  (short-dashed line) given by equations (51) and (52). The scattering rate decreases at large  $\tilde{r}$  near the outer boundary.

flow. The solution presents the same qualitative features as the coherent scattering solution for the Hubble velocity profile, in particular the peak in intensity that drifts redwards from line centre further from the source, although significant quantitative differences are apparent. The frequency displacement of the peak increases more slowly with radius than in the Hubble velocity case, a result of a reduced velocity across the range in radius which is less efficient in redshifting photons.

The computations expended by the Monte Carlo code are significantly reduced if we may assume the photon occupies only a single frequency bin between scattering or boundary crossing events, which we take to be that corresponding to the ‘final’ frequency prior to scattering. In a Hubble velocity field the comoving frequency changes with path length  $\lambda$  as  $x = x_{\text{em}} - (H/b)\lambda$ , and the approximate treatment is accurate in the limit that the path length between scattering or boundary crossing events satisfies  $\delta\lambda \ll b\Delta x/H$ , where  $\Delta x$  is the frequency bin size, a condition which is certainly satisfied in our examples for distances between scattering events at line centre important in determining the scattering rate. For a general velocity profile this condition is replaced by  $\delta\lambda \ll b\Delta x/|dV/dr|$ , and so this approximate treatment is valid as long as  $V(r)$  does not change too rapidly. We obtained a Monte Carlo solution for the coherent scattering problem which is compared with our ray/moment solution in Fig. 20. The Monte Carlo scattering rate is compared with that determined from the equivalent ray/moment solution in Fig. 21. Well interior to the outer boundary, the scattering rate is boosted by up to an order of magnitude compared with the expected rate for a Hubble velocity profile, given approximately by  $\tilde{P}_\alpha^{\text{diff}}$ . Near the outer boundary, where the velocity gradient well exceeds the Hubble constant, the scattering rate dips below  $\tilde{P}_\alpha^{\text{diff}}$ .

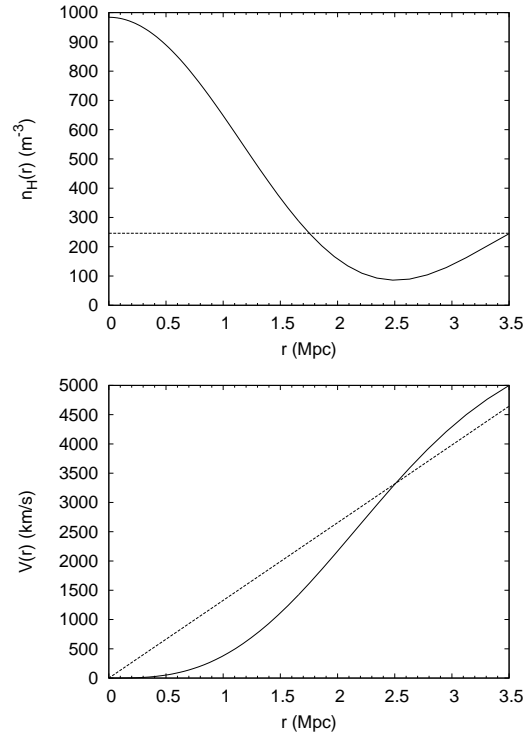


**Figure 22.** Density profile (solid line, upper panel) and velocity profile (solid line, lower panel) given by equations (64) and (65) respectively with amplitude  $\Delta_0 = 3$  and compared with the corresponding uniform density or Hubble velocity profile at  $z = 10$  (dashed lines).

### 5.3 Spherical Perturbation in Density and Velocity

In this section we examine the scattering rate resulting from a perturbation to the uniform density and Hubble velocity profiles of a homogeneous expanding medium. We assume a spherically symmetric overdensity of the form

$$\begin{aligned} \delta(r) &= \Delta_0 j_0(kr) \\ \Rightarrow n_H(r) &= n_H(z)[1 + \Delta_0 j_0(kr)] \end{aligned} \quad (64)$$

where  $j_0(x) = (\sin x)/x$  is the zeroth-order spherical Bessel function,  $\Delta_0$  is the amplitude of the perturbation and the value of  $k$  is taken to be  $2\pi/R$ , where  $R$  is the radius of the outer boundary. A restriction on the amplitude follows from the physical requirement that  $\delta \geq -1$ , which then requires that  $\Delta_0 \lesssim 5$ . The corresponding self-consistent perturbation in the peculiar velocity follows from the linear regime equation  $\delta = -(1/H)\nabla \cdot \mathbf{v}_p$  which in spherical symmetry is solved for  $\delta = \Delta_0 j_0(kr)$  and the boundary condition that the velocity vanishes at  $r = 0$  by

$$\begin{aligned} v_p &= -\frac{\Delta_0 H(z)}{k} j_1(kr) \\ \Rightarrow V(r) &= Hr + v_p = H(z) \left[ r - \frac{\Delta_0}{k} j_1(kr) \right] \end{aligned} \quad (65)$$

where  $j_1(x) = (\sin x)/x^2 - (\cos x)/x$  is the first-order spherical Bessel function.

We solve the radiative transfer problem for a continuum source subject to a scattering medium with the perturbed



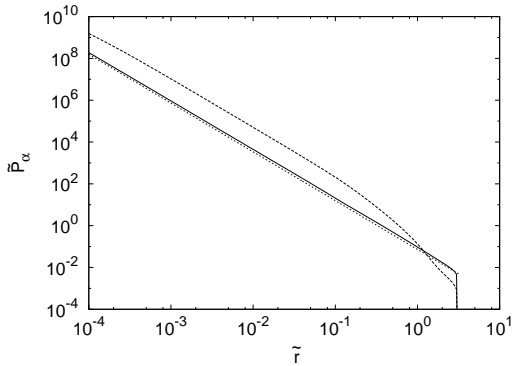


**Figure 23.** Scaled scattering rate for a spherical perturbation with the density profile equation (64) and velocity profile equation (65), with  $k = 2\pi/R$ ,  $\tilde{R} = 10^{0.5}$  and  $x_m = 6 \times 10^4$ , for  $\Delta_0 = 0.5$  (solid line) and  $\Delta_0 = 2.9$  (dashed line). The scattering rates are derived from numerical integration of the ray/moment equation method for coherent scattering. For comparison the rate in the diffusion approximation for a uniformly expanding homogeneous medium is also shown (short-dashed line).

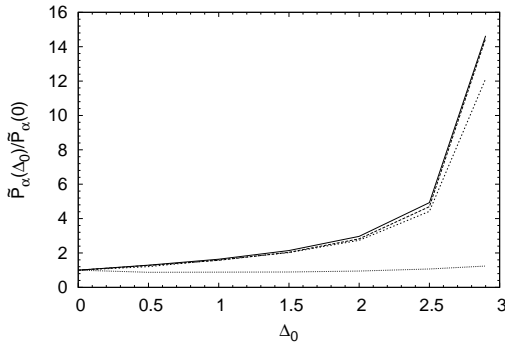


**Figure 24.** Scaled scattering rate for a spherical perturbation with the density profile equation (64) and velocity profile equation (65), with  $k = 2\pi/R$ ,  $\tilde{R} = 10^{0.5}$  and  $x_m = 6 \times 10^4$ , as a function of the perturbation amplitude  $\Delta_0$  and normalised by the value for  $\Delta_0 = 0$ , at different radii given by  $\tilde{r} = 10^{-3}$  (solid line,  $\tilde{P}_\alpha(0) = 7.2 \times 10^5$ ),  $10^{-2}$  (long-dashed line,  $\tilde{P}_\alpha(0) = 3.5 \times 10^3$ ),  $10^{-1}$  (short-dashed line,  $\tilde{P}_\alpha(0) = 17$ ) and  $10^0$  (dotted line,  $\tilde{P}_\alpha(0) = 0.11$ ). The scattering rates are derived from numerical integration of the ray/moment equation method for coherent scattering.

density and velocity profiles of equations (64) and (65), respectively, using the ray/moment equation solution method assuming coherent scattering in a medium with temperature  $T = 10$  K. We note that a further restriction on the perturbation amplitude  $\Delta_0$  follows from requiring a monotonic velocity field, with  $V(r) \geq 0$  and  $V'(r) \geq 0$  for all  $r$ , necessary to apply the moment equation solution method. The resulting constraint is  $\Delta_0 \leq 3$ , corresponding to a vanishing velocity gradient at small  $r$ . While such large values of  $\Delta_0$  are no longer in the linear regime, used to derive equation (65), the form permits an exploration of the effect of the shape of the velocity field on the transport of the Ly $\alpha$  photons.

The hydrogen density and velocity profiles corresponding to our assumed cosmological parameters at  $z = 10$ , an outer boundary  $R = 10^{0.5} r_* \simeq 3.5$  Mpc and a perturbation

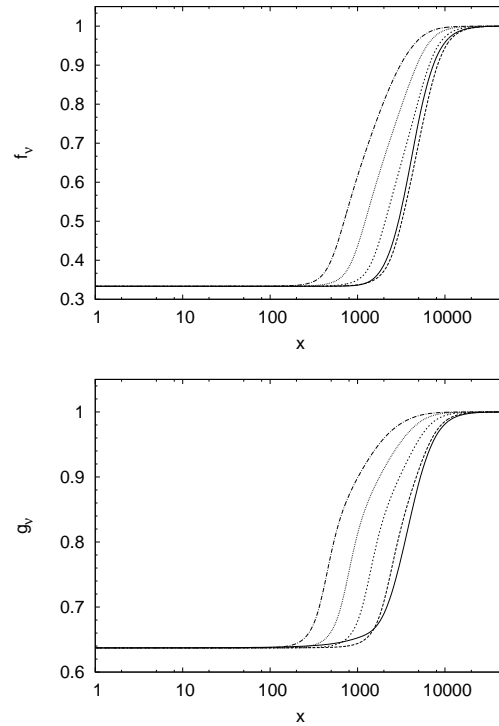


**Figure 25.** Eddington factors  $f_\nu$  (upper panel) and  $g_\nu$  (lower panel) for a spherical perturbation with the density profile equation (64) and velocity profile equation (65) for  $\Delta_0 = 2.9$ , derived from numerical integration of the ray/moment equations assuming coherent scattering. The factors are shown at  $\log_{10} \tilde{r} = 0$  (solid line),  $\log_{10} \tilde{r} = -0.5$  (long-dashed line),  $\log_{10} \tilde{r} = -1.0$  (short-dashed line),  $\log_{10} \tilde{r} = -1.5$  (dotted line) and  $\log_{10} \tilde{r} = -2.0$  (dot-dashed line). The factors take on the values  $f_\nu \simeq 1/3$  and  $g_\nu \gtrsim 3/5$ , close to the values expected for the linear approximation  $I_\nu \simeq J_\nu + 3H_\nu \mu$ , across the line centre, and  $f_\nu = g_\nu = 1$  far in the wings expected for free-streaming radiation.

with  $\Delta_0 = 3$ , are shown in Fig. 22. The scattering rate as a function of distance from the source is shown in Fig. 23 for  $\Delta_0 = 0.5$  and  $2.9$ . While a small amplitude perturbation has a correspondingly small effect on the scattering rate, the rate is substantially boosted for  $\Delta_0 \lesssim 3$ . The dependence of the scattering rate on the perturbation amplitude for  $\Delta_0 < 3$  is shown at various radii in Fig. 24. The scattering rate scales linearly with the amplitude for small values,  $\Delta_0 \lesssim 1$ , but increases more rapidly with larger values. It grows exponentially as  $\Delta_0 \rightarrow 3$ , a result of a vanishing velocity gradient for  $r \rightarrow 0$  (cf. Figs 19 and 21). Clearly a small velocity gradient near the source is able to substantially boost the scattering rate over a wide range of radii compared with the case of uniform Hubble flow.

The solutions obtained from the solving the ray/moment equations have generally justified the linear approximation  $I_\nu \simeq J_\nu + 3H_\nu \mu$  in  $\mu$ , for which the first two Eddington factors are  $f_\nu = 1/3$  (the Eddington approximation) and  $g_\nu = 3/5$ . For a linear velocity field, only  $f_\nu$  is required, as the terms involving  $N_\nu$  in equation (18) cancel. The perturbed flow here allows a check on  $g_\nu$ . The Eddington factors are shown in Fig. 25. They take on the values  $f_\nu = 1/3$  and  $g_\nu \gtrsim 3/5$  over a broad frequency region across the line centre, and the values  $f_\nu = g_\nu = 1$

far in the wings, as expected for free-streaming radiation. On the outer boundary,  $h_\nu \gtrsim 0.7$  over a similarly broad region across the line centre, allowing closure of the moment equations. The value corresponds to a single dominant escaping stream of radiation with  $\mu \simeq 2^{-1/2}$ . This would correspond to  $f_\nu = g_\nu = 1/2$ , close to the computed values on the outer boundary of  $f_\nu \simeq 0.5$  and  $g_\nu \gtrsim 0.6$ .

## 6 CONCLUSIONS

The 21 cm signatures of the first luminous objects are dependent upon the Ly $\alpha$  scattering rate, which is necessary to decouple the H I spin temperature from the CMB temperature through the Wouthuysen-Field effect in the diffuse IGM during the early stages of reionization and so render the hydrogen detectable against the CMB via 21 cm observations. Realistic studies of Ly $\alpha$  scattering caused by the first sources during the EoR will need to make use of three-dimensional density and velocity fields derived from cosmological simulations, and treat the time-dependent radiative transfer of photons contributed from multiple sources of finite lifetime, the detailed properties and spatial distributions of which are largely uncertain and will have to be extrapolated from lower-redshift observations or estimated from galaxy formation simulations. Together with the extensive effort currently underway in removing radio foregrounds and isolating the signal of the EoR, these detailed analyses will be critical in predicting and interpreting future 21 cm tomographic observations made by existing and future radio interferometric arrays, such as LOFAR and SKA.

We develop two methods for solving the radiative transfer equation for resonance line photons in spherically symmetric systems, and apply them to idealized problems relevant to the 21 cm signature of the IGM. We consider five classes of problems corresponding to a point source emitting either emission line or continuum radiation in an expanding medium, allowing for a uniformly expanding homogeneous medium, a uniformly expanding medium with an overdense shell around the source, a homogeneous medium with a quadratic velocity profile, and a medium with a self-consistent density and velocity perturbation around the source. A static medium test problem is also treated. Since these problems may serve as useful tests of Monte Carlo schemes, we provide their solutions in machine-readable format (Appendix D).

Following Mihalas et al. (1975) and Mihalas et al. (1976), the first method is based on solving the ray and angular moment forms of the comoving frame radiative transfer equation in a spherically symmetric medium subject to a monotonic velocity profile  $V(r)$ , where  $V \geq 0$  and  $V' \geq 0$  for all  $r$  (see Section 2.1). We described general boundary conditions required by these methods in order to treat the radiative transfer of Ly $\alpha$  scattering in a cosmological context. We also obtained an efficient prescription for the finite difference representation of the source function for partial frequency redistribution based on the diffusion approximation.

We compare our results with Monte Carlo solutions to the radiative transfer equation using an implementation that determines the Ly $\alpha$  radiation mean intensity from the accumulated path lengths of the photons within a given vol-

ume and frequency range. This greatly improves the accuracy over a technique that uses spatial and frequency bin crossings to estimate the intensity. For 200 logarithmically-spaced grid zones covering three decades in radius, the noise level in the scattering rate is kept under 10 per cent per radial bin using  $2 \times 10^5$  photon packets. The code computes the Doppler redistribution of the frequencies upon scattering both directly and by interpolating on the RII redistribution function. The latter speeds the computations by a factor of a few, but requires a grid tailored to a specific application, so lacks generality.

In Section 4 we validated our schemes using various test problems for resonance line photon scattering in spherical symmetry, including: (i) Ly $\alpha$  scattering in an optically thick static sphere (Dijkstra et al. 2006) and (ii) the Ly $\alpha$  scattering halo of a monochromatic Ly $\alpha$  point source in a uniformly expanding homogeneous medium (Loeb & Rybicki 1999). We found the ray and moment method results agreed with the analytic solutions, at least in the optically thick regime where the analytic solutions are valid, while in case (ii) our solution matched the Monte Carlo solution found by Loeb & Rybicki. A final test problem was described for a continuum source in a uniformly expanding homogeneous medium. We utilised the analytic solution of Loeb & Rybicki (1999), valid in the zero-temperature diffusion approximation, as a Green's function to obtain the equivalent solution for a flat source spectrum in the diffusion approximation. The solution gives a radial profile for the Ly $\alpha$  scattering rate that varies as  $r^{-7/3}$ , steeper than the free-streaming dependence  $r^{-2}$ , and the same dependence found by other authors in Monte Carlo studies of this problem. Our analytic solution also allows for a maximum frequency cutoff from the source; both of our numerical methods recover the effects of the cutoff. The photon production rate between Ly $\alpha$  and Ly $\beta$  required to couple the spin temperature to the gas kinetic temperature is found to be  $\dot{N}_{\alpha, \text{th}}^{\text{cont}} \simeq 4.39 \times 10^{55} [(1+z)/11] r_{\text{Mpc}}^{7/3} \text{ s}^{-1}$ , where  $r_{\text{Mpc}}$  is the distance from the source in megaparsecs. This is less demanding than for an emission-line source by several orders of magnitude at a distance of 1 Mpc.

We solve the test problem of a continuum source in a uniformly expanding homogeneous IGM numerically, outside of the diffusion limit, using our ray/moment and Monte Carlo methods for spherical symmetry. In suitable spherically symmetric problems such as this test problem, the combined ray/moment equation solution method may be used to quickly produce noise-free results, in contrast to the Monte Carlo approach for a practical number of photon packets. For more general situations, the Monte Carlo method is more readily extended to treat cartesian grids with general configurations of sources and arbitrary density, temperature and peculiar velocity fields within the scattering medium.

For precision results, however, a grid-based scheme such as the method presented here may be desirable. In this case, the diffusion approximation may be used as an inner boundary condition on the surface of an inner core region. For non-monotonic velocity fields, the problem would need to be divided into monotonic flow regions and pieced together. It may not, however, be necessary to solve the coupled moment and ray equations to obtain the scattering rates. We find for all solutions that the linear approximation  $I_\nu \simeq J_\nu + 3H_\nu \mu$

holds to high accuracy over a very broad frequency region (at least 100 Doppler widths for  $T = 10$  K gas) across the line centre, giving the Eddington approximation value  $f_\nu \simeq 1/3$ , for linear flow fields before converging to the free-streaming value  $f_\nu = 1$  far in the wings. Allowing for a perturbed velocity flow gives close to the expected value  $g_\nu = 3/5$  over a similarly broad region. This considerably simplifies the radiative transfer computation, as solving the ray equation may be circumvented, requiring only solutions to the moment equations.

We found frequency redistribution produces solutions with different features across the line centre compared with the coherent scattering case near the source, resulting in variations in the scattering rate of up to  $\sim 50$  percent about the coherent scattering results. Further from the source the solutions for a homogeneous expanding IGM were found to agree closely with the solution for coherent scattering, and roughly follow the analytically predicted  $r^{-7/3}$  radial dependence out to  $\tilde{r} \simeq 1$ , beyond which the diffusion approximation breaks down. For  $\tilde{r} > 1$ , the scattering rate more nearly approaches the free-streaming value  $1/4\pi\tilde{r}^2$  before becoming causally truncated.

Recoils are found to suppress the scattering rate by approximately 20 percent for a medium at a temperature of  $T = 10$  K, in good agreement with estimates based on the diffusion approximation solution for the radiation produced by a uniform and isotropic distribution of sources in a uniformly expanding homogeneous medium. Our computations extend the result beyond the diffusion approximation, and show that nearly the same suppression factor applies for an isolated source. Very near the source, frequency redistribution modifies the suppression factor by up to 15 percent.

In Section 5 we examined the continuum source Ly $\alpha$  scattering problem allowing for inhomogeneities in the surrounding scattering medium, namely an overdense shell and a quadratic velocity profile. We found substantial deviations in the profile of the Ly $\alpha$  scattering rate in each case compared with a homogeneous medium. The overdense shell produces not only an enhancement of the Ly $\alpha$  scattering rate within the shell, but boosts the scattering rate between the shell and the source as well as a consequence of backscattering. A shadowed region with a deficit in the scattering rate compared with the homogeneous medium solution extends beyond the shell some distance before recovering to the homogeneous medium value. The scattering rate produced by the quadratic velocity profile is enhanced over the rate for the corresponding linear velocity profile, except near the outer boundary, where the rate is lower.

As a less-contrived example of an inhomogeneous medium we considered a spherically symmetric density and velocity perturbation in a uniformly expanding homogeneous IGM that satisfies the linear continuity equation. We found that the resulting scattering rate increases nonlinearly with increasing values of the perturbation amplitude for perturbations beginning to become nonlinear, and grows exponentially with the amplitude once nonlinear as the velocity profile flattens near the source. We infer that the Ly $\alpha$  scattering rate will depend sensitively on the velocity structure of the IGM.

## APPENDIX A: Ly $\alpha$ SCATTERING SOURCE FUNCTION FOR THE MOMENT EQUATIONS

A particularly useful representation of the source function for resonance-line scattering results from assuming the diffusion approximation or Fokker-Planck approximation (Rybicki & dell’Antonio 1994), in which a Taylor expansion of  $J_\nu(r)$  under the integral in equation (33) gives

$$S_\nu(r) = J_\nu(r) + \frac{(\Delta\nu_D)^2}{2\varphi(\nu)} \frac{\partial}{\partial\nu} \left[ \varphi(\nu) \frac{\partial J_\nu(r)}{\partial\nu} \right] + \epsilon \frac{\Delta\nu_D}{\varphi(\nu)} \frac{\partial}{\partial\nu} [\varphi(\nu) J_\nu(r)] \quad (\text{A1})$$

where we have included an additional correction term proportional to the recoil parameter  $\epsilon = h\nu_\alpha/(\sqrt{2k_B T m c^2}) = 0.025(T/\text{K})^{-1/2}$ , arising from the effect of atomic recoil on the frequency redistribution function (Field 1959b; Basko 1978). In this section we will describe how this form of the source function is represented in the discretised system of moment equations.

We assign a frequency grid given by the discrete set  $\{\nu_k\}$ ,  $k = 1, 2, 3, \dots, \text{NF}$ , where  $\nu_1 = \nu_{\text{max}}$  is the bluest frequency and successive values of  $k$  denote redder frequencies:

$$\nu_1 = \nu_{\text{max}} > \nu_2 > \nu_3 > \dots > \nu_{\text{NF}}. \quad (\text{A2})$$

The radius grid is given by  $\{r_d\}$ ,  $d = 1, 2, 3, \dots, \text{ND}$ , where  $r_1 = R$  and  $r_{\text{ND}} = R_C$ ; increasing values of the depth index  $d$  denote greater depths with respect to the ‘surface’ of the system at  $r = R$ :

$$r_1 = R > r_2 > r_3 > \dots > r_{\text{ND}} = R_C. \quad (\text{A3})$$

In terms of the discrete grids in  $\nu$  and  $r$ , we write the source function  $S_{k,d} \equiv S_{\nu_k}(r_d)$  as a quadrature sum:

$$S_{k,d} = \sum_{k'=1}^{\text{NF}} \mathcal{R}_{k',k,d} J_{k',d} \quad (\text{A4})$$

where  $J_{k',d} \equiv J_{\nu_{k'}}(r_d)$ . We require the coefficients  $\mathcal{R}_{k',k,d}$  for  $k, k' = 1, 2, \dots, \text{NF}$  and  $d = 1, 2, \dots, \text{ND}$ , the values of which are determined by a suitable discretised description of equation (A1).

In a system with a uniform temperature it is preferable to work with the dimensionless frequency variable  $x = (\nu - \nu_\alpha)/\Delta\nu_D$ , the offset from line centre in Doppler widths, and rewrite radiation quantities as e.g.  $J(x, r) = (\Delta\nu_D) J_\nu(r)$ . Similar relations hold for higher order moments and the source function. In these units we define  $R(x', x) = (\Delta\nu_D)^2 R(\nu', \nu)$ , while the line absorption profile is expressed as  $\phi(x) = (\Delta\nu_D) \varphi(\nu)$ . The source function and its diffusion approximation expansion may then be expressed as

$$S(x, r) = \frac{1}{\phi(x)} \int R(x', x) J(x', r) dx' = J(x, r) + \frac{1}{2\phi(x)} \frac{\partial}{\partial x} \left[ \phi(x) \frac{\partial J(x, r)}{\partial x} + 2\epsilon\phi(x) J(x, r) \right]. \quad (\text{A5})$$

The frequency derivative terms are represented using a centred finite difference scheme, and the coefficients multiplying values of  $J_{k,d} \equiv J(x_k, r_d)$  are compared with equation (A4)

to obtain the values of  $\mathcal{R}_{k',k,d}$ :

$$\begin{aligned}\mathcal{R}_{k',k} &= \left[1 - \frac{\phi_{k-1} + \phi_{k+1}}{8\phi_k(\Delta x)^2}\right] \delta_{k',k} \\ &+ \left[\frac{\phi_{k-1}}{8\phi_k(\Delta x)^2}\right] \delta_{k',k-2} + \left[\frac{\phi_{k+1}}{8\phi_k(\Delta x)^2}\right] \delta_{k',k+2} \\ &+ \epsilon \left[\frac{\phi_{k-1}}{2\phi_k\Delta x}\right] \delta_{k',k-1} - \epsilon \left[\frac{\phi_{k+1}}{2\phi_k\Delta x}\right] \delta_{k',k+1}, \quad (\text{A6})\end{aligned}$$

where we have noted that any dependence on radius is removed for a uniform temperature medium, so that  $\mathcal{R}_{k',k,d} \rightarrow \mathcal{R}_{k',k}$ . Otherwise a radial dependence must be introduced to the discretised values of  $\phi$ .

## APPENDIX B: MONTE CARLO METHOD

We will assume a uniform temperature medium to allow use of the scaled frequency offset  $x$  defined for a unique value of the Doppler width  $\Delta\nu_D$ , although the method is easily adapted to a variable temperature  $T(r)$  by formulating it in terms of the frequency variable  $\nu$ . We consider a photon packet emitted/scattered with comoving frequency  $x_{\text{em}}$  at position  $\mathbf{r}_{\text{em}}$  in a direction denoted by unit vector  $\hat{\mathbf{k}}$ . In spherical symmetry it is sufficient to designate the radius of emission  $r_{\text{em}}$  and the angle to the local normal  $\theta_{\text{em}}$ , the latter having cosine  $\mu_{\text{em}} \equiv \cos\theta_{\text{em}} = \hat{\mathbf{k}} \cdot \mathbf{r}_{\text{em}}/r_{\text{em}}$ . The path of the photon packet prior to the next scattering event is given by  $\mathbf{r} = \mathbf{r}_{\text{em}} + \lambda\hat{\mathbf{k}}$ , where  $\lambda$  is the distance along the path of the packet. We consider a ‘projected photon packet path’ corresponding to the range  $\lambda = -\infty \rightarrow \infty$ , having impact parameter  $r_{\text{min}}$  defined as the minimum distance from the origin:  $r_{\text{min}} = r_{\text{em}} \sin\theta_{\text{em}} = r_{\text{em}}(1 - \mu_{\text{em}}^2)^{1/2}$ . A spherical boundary of radius  $r > r_{\text{min}}$  will be intersected by the projected photon packet path at distances along the path  $\lambda_{\pm}$  determined from solving  $\mathbf{r} \cdot \mathbf{r} = r^2$  with  $\mathbf{r} = \mathbf{r}_{\text{em}} + \lambda\hat{\mathbf{k}}$ :

$$\begin{aligned}\lambda_{\pm}(r) &= -\hat{\mathbf{k}} \cdot \mathbf{r}_{\text{em}} \pm \left[r^2 - r_{\text{em}}^2 + (\hat{\mathbf{k}} \cdot \mathbf{r}_{\text{em}})^2\right]^{1/2} \\ &= -\mu_{\text{em}}r_{\text{em}} \pm (r^2 - r_{\text{min}}^2)^{1/2} \quad (\text{B1})\end{aligned}$$

where obviously only positive values denote possible intersections of the actual photon packet path with the sphere. At the radius  $r$ , the corresponding angle to the local normal is given by  $\mu = \hat{\mathbf{k}} \cdot \mathbf{r}/r$  where  $\mathbf{r} = \mathbf{r}_{\text{em}} + \lambda_{\pm}\hat{\mathbf{k}}$ :

$$\begin{aligned}\mu_{\pm}(r) &= (\mu_{\text{em}}r_{\text{em}} + \lambda_{\pm})/r \\ &= \pm [1 - (r_{\text{min}}/r)^2]^{1/2}. \quad (\text{B2})\end{aligned}$$

At any point  $\mathbf{r}$  along its path, the packet will have a comoving frequency corresponding to the same lab frame frequency as  $x_{\text{em}}$ , and thus

$$\begin{aligned}x(r) &= x_{\text{em}} - \mathbf{V}(\mathbf{r}) \cdot \hat{\mathbf{k}}/b + \mathbf{V}(\mathbf{r}_{\text{em}}) \cdot \hat{\mathbf{k}}/b, \\ &= x_{\text{em}} - \mu(r)V(r)/b + \mu_{\text{em}}V(r_{\text{em}})/b \quad (\text{B3})\end{aligned}$$

where  $\mu$  describes the angle to the local normal of the sphere at  $\mathbf{r}$ . For the special case of a Hubble-flow velocity field, i.e.  $V(r) = Hr$ , this reduces to

$$\begin{aligned}x(r) &= x_{\text{em}} - (\mu r - \mu_{\text{em}}r_{\text{em}})H/b \\ &= x_{\text{em}} - \lambda H/b \quad (\text{B4})\end{aligned}$$

where the content of the brackets simplifies following equation (B2); the frequency shift is linearly dependent on the

distance  $\lambda$  travelled along the path. We use these equations to record the frequency, path length and the angle to the local normal of the photon packet as it crosses a series of spherical boundaries of radius  $\{r_d\}$ , the values of which comprise a radial grid across which we seek the mean intensity  $J_{\nu}(r)$  and the scattering rate  $P_{\alpha}(r)$ .

The packet is scattered when the accumulated optical depth  $\tau$  reaches a sufficiently large value. This optical depth is chosen according to an exponential probability distribution  $e^{-\tau}$ , i.e.  $\tau = -\ln R$  for a uniform deviate  $R$ . For a Ly $\alpha$  scattering opacity  $\chi_{\nu} = n_{\text{H}}\sigma\varphi(\nu)$ , the differential optical depth accumulated along a length  $d\lambda$  may be expressed as  $d\tau = n_{\text{H}}\sigma[\phi(x)/\Delta\nu_D]d\lambda$ . The total optical depth is the integral along the path. For a static medium of constant temperature and neutral hydrogen density  $n_{\text{H}}$ , this integral is trivial:  $\lambda = \tau\Delta\nu_D/[n_{\text{H}}\sigma\phi(x)]$ ; however, for a non-static medium the frequency  $x$  varies as in equation (B3) and no simple  $\tau$ -dependence may be obtained as a function of  $\lambda$ .

A less rigid approach is to assume the density, temperature and velocity of the medium are essentially constant across shells, as in the Monte Carlo code of Dijkstra et al. (2006). Under these circumstances the comoving frequency of the packet changes in steps as the path crosses shell boundaries, and the optical depth between two boundaries behaves as in the uniform static case. The optical depth between boundaries at distances  $\lambda_d$  and  $\lambda_{d+1}$  along the packet path is

$$\Delta\tau = \frac{\sigma n_{\text{H}}(r_d)\phi(x_d)}{\Delta\nu_D}|\lambda_{d+1} - \lambda_d| \quad (\text{B5})$$

where the subscript  $d$  indicates evaluation at the intersection with the boundary of radius  $r_d$ , using equations (B1) and (B3). The packet is permitted to progress along its path until the sum of the values of  $\Delta\tau$  exceeds the randomly selected total optical depth, at which stage the packet is scattered. If the optical depth corresponds to a total distance  $\lambda_{\text{max}}$  along the path of the packet, the packet is moved to a new radius  $r$  given by applying the cosine rule to the triangle of sides  $r_{\text{em}}$ ,  $r$  and  $\lambda_{\text{max}}$ :

$$r = (r_{\text{em}}^2 + \lambda_{\text{max}}^2 + 2\mu_{\text{em}}r_{\text{em}}\lambda_{\text{max}})^{1/2}. \quad (\text{B6})$$

Upon scattering, the photon packet is re-emitted with a new direction  $\mu_{\text{em}}$  and a new frequency  $x_{\text{em}}$ .

We generally assume isotropic scattering, for which the emitted direction is obtained using  $\mu_{\text{em}} = 2R - 1$  for a uniform random deviate  $R$ . We determined the emitted frequency from the well-known frequency redistribution function  $R_{\text{II}}(x', x)$  (Mihalas 1978) using a numerical lookup table method. The method uses the probability distribution  $p(x|x') = R_{\text{II}}(x', x)/\phi(x)$  for the output/emitted frequency  $x$  given the input/absorbed frequency  $x'$ , and is described in some detail in Higgins (2012). An alternative method that is more adaptable and has been widely adopted by other authors is based on selecting the scattering atom thermal velocity components and calculating the output frequency directly from the resulting Doppler shifts (Chen & Miralda-Escudé 2004). We found our lookup table method to speed up the Monte Carlo computations by a factor of approximately 3 compared with the direct Doppler shift computation method, however the required pre-calculation can become cumbersome.

We estimate the mean intensity using the method of

Lucy (1999), based on the time-averaged number density of photons in a cell of a given volume. We tailor the method to solve problems in spherical symmetry by adopting a cell of volume  $V$  corresponding to the volume of the shell between two radial grid-spheres of radius  $r$  and  $r + \Delta r$ , given by  $V \simeq 4\pi r^2 \Delta r$ . If a Monte Carlo photon packet travels a distance  $\delta\lambda$  in the shell between two scattering events, the packet occupies the shell for a time  $\delta t = \delta\lambda/c$  and contributes to the specific number density within the shell, at the frequency of the packet, the increment  $V^{-1}\delta t/\Delta t$  where the quantity  $\Delta t$  is the physical time represented by the entire Monte Carlo run. The total number density  $n_\nu(r) \Delta\nu$  comes from the sum of all the values of  $\delta\lambda$  between any two general ‘events’, which may be a scattering event, a boundary crossing or redshifting/blueshifting between adjacent frequency bins, arising from packets travelling within the shell while having frequency within the range  $[\nu, \nu + \Delta\nu]$ . The mean intensity is then computed from  $J_\nu = [c/(4\pi)]n_\nu$  as

$$J_\nu(r) = \frac{1}{4\pi V(\Delta\nu)(\Delta t)} \sum_{\text{events}} \delta\lambda(\nu, r). \quad (\text{B7})$$

The distances  $\delta\lambda$  between scattering events and/or boundary crossings are computed by following the intersections of the path of a photon packet with the radial grid. For a packet that travels a short distance  $\lambda_{\text{max}}$  before scattering, so that the entire path is contained within the shell at  $r$  and the packet frequency remains within the frequency bin at  $\nu$ , we take  $\delta\lambda = \lambda_{\text{max}}$ . However, if the path of the packet crosses shell boundaries or causes redshifting/blueshifting between adjacent frequency bins, it is necessary to separate the total path length  $\lambda_{\text{max}}$  into multiple values of  $\delta\lambda(\nu, r)$  at the appropriate radii and/or frequencies. For packets crossing shell boundaries the  $\delta\lambda$  values are obtained from differencing the distances along the path of the packet at which the shell boundary intersections defined by equation (B1) occur. For a packet path defined by  $r_{\text{em}}$  and  $\mu_{\text{em}}$  the choice of  $\lambda_+$  or  $\lambda_-$  is given by either of two sequences, distinguished by the sign of  $\mu_{\text{em}}$ : (i) for a packet emitted in an ‘outward’ direction with  $\mu_{\text{em}} > 0$ , only  $\lambda_+$  potentially represents a boundary crossing as  $\lambda_- < 0$  and the packet may potentially cross every boundary with radius  $r > r_{\text{em}}$ , and (ii) for a packet emitted ‘inwards’ with  $\mu_{\text{em}} < 0$ , the solution  $\lambda_+ > 0$  for all  $r > r_{\text{min}}$  and  $\lambda_- > 0$  for  $r_{\text{min}} < r < r_{\text{em}}$  and thus the potential path of the packet will cross shell boundaries of decreasing radii from  $r_{\text{em}}$  down to  $r_{\text{min}}$  with  $\lambda$  given by  $\lambda_-$ , then increasing radii from  $r_{\text{min}}$  upwards with  $\lambda$  given by  $\lambda_+$ . The values of  $\delta\lambda$  are given by the differences in sequential values of  $\lambda$ , although we only follow the sequence in each case until the packet is scattered. Some additional calculation is needed for non-static media in order to treat redshifting/blueshifting between adjacent frequency bins while a packet is ‘in transit,’ i.e. in between scattering events and/or boundary crossings. We discuss this in applications to particular problems within the main text.

As an alternative to the summed path-length estimator for the mean intensity  $J_\nu(r)$ , we describe an estimator for the specific intensity  $I_\nu(r, \mu)$ . From the definition of specific intensity we write the differential number of photons in the frequency range  $[\nu, \nu + d\nu]$  crossing the boundary at  $\mathbf{r}$  within solid angle  $d\omega$  about direction  $\hat{\mathbf{n}}$ , normal to area  $dA$ , in time  $dt$  as  $dN = I_\nu(\mathbf{r}, \hat{\mathbf{n}}) dA d\omega d\nu dt$ . The differential solid angle is simply  $d\omega = |d\mu| d\phi$  and the area  $dA$  normal to

$\hat{\mathbf{n}}$  is related to the differential area of the boundary  $dS$  by  $dA = |\mu| dS$ . The total number  $N(r, \mu, \nu)$  of photons within frequency range  $[\nu, \nu + d\nu]$  crossing the boundary of radius  $r$  within angular range  $[\mu, \mu + d\mu]$ , is then equal to the integral of  $dN$  over the azimuthal angle and the boundary surface:  $N(r, \mu, \nu) = I_\nu(r, \mu) |\mu| (\oint dS) (\int d\phi) d\mu d\nu dt$ , or

$$I_\nu(r, \mu) = \frac{N(r, \mu, \nu)}{8\pi^2 r^2 |\mu| (\Delta\mu)(\Delta\nu)(\Delta t)} \quad (\text{B8})$$

where  $\Delta\mu$  and  $\Delta\nu$  are the bin sizes in angle and frequency, and  $\Delta t$  is again the physical time represented by the Monte Carlo run which is related to the total number of photons emitted by the source. The quantity  $N(r, \mu, \nu)$  is determined simply by incrementing an appropriate counter every time a photon packet crosses the shell at  $r$ . This method provides an alternative means of determining the mean intensity  $J_\nu$ , which follows from angular integration, however, as it samples only those packets that cross radial shells, we found it to be a less efficient means of estimating the mean intensity at line centre, where the path lengths are short, compared with the summed path-length method. This method is, however, required to determine higher-order angular moments of the intensity.

## APPENDIX C: ANALYTIC SOLUTIONS FOR A HOMOGENEOUS EXPANDING MEDIUM

### C1 Ly $\alpha$ Source

In this section we review the derivation of the solution for a Ly $\alpha$  point source in a homogeneous expanding medium (Loeb & Rybicki 1999). This solution provides the basis for the derivation of the corresponding solution for a continuum source.

We rewrite equation (1) in a dimensionless form using the frequency and radius variables previously described in Section 4.2:

$$\mu \frac{\partial \tilde{I}}{\partial \tilde{r}} + \frac{1 - \mu^2}{\tilde{r}} \frac{\partial \tilde{I}}{\partial \mu} + \tilde{\alpha} \left[ 1 - \mu^2 + \mu^2 \left( \frac{d \ln V}{d \ln r} \right) \right] \frac{\partial \tilde{I}}{\partial \tilde{\nu}} = -\tilde{\chi} \tilde{I} + \tilde{\eta} + \delta(\tilde{\nu}) \frac{\delta(\tilde{r})}{(4\pi \tilde{r})^2} \quad (\text{C1})$$

where  $\tilde{\alpha} \equiv V/[H(z)r]$ ,  $\tilde{\chi} \equiv r_* \chi_\nu$  and  $\tilde{\eta} \equiv (r_*/I_*^l) \eta_\nu$ . In the idealised zero-temperature limit assumed by Loeb & Rybicki, atoms have zero thermal velocity and RII redistribution becomes coherent in the frame of the observer, while the line profile is that of natural broadening alone. Coherent scattering in an expanding medium means photons emitted at  $\nu = \nu_\alpha$  can only get redder, and thus the wing form of the opacity applies while the emissivity reduces to  $\eta_\nu = \chi_\nu J_\nu$ . They assumed a velocity profile for the H I medium given by the Hubble expansion,  $V(r) = Hr$ ; note that for this linear scaling the expression in square brackets in equation (C1) reduces to unity and  $\tilde{\alpha} = 1$ . The zeroth and first order angular moment equations are given by:

$$\frac{1}{\tilde{r}^2} \frac{\partial(\tilde{r}^2 \tilde{H})}{\partial \tilde{r}} + \frac{\partial \tilde{J}}{\partial \tilde{\nu}} = \delta(\tilde{\nu}) \frac{\delta(\tilde{r})}{(4\pi \tilde{r})^2}, \quad (\text{C2})$$

$$\frac{\partial \tilde{K}}{\partial \tilde{r}} + \frac{3\tilde{K} - \tilde{J}}{\tilde{r}} + \frac{\partial \tilde{H}}{\partial \tilde{\nu}} = -\frac{\tilde{H}}{\tilde{\nu}^2}. \quad (\text{C3})$$

A solution may be obtained in the Eddington approximation

$\tilde{K} = \tilde{J}/3$ . In the diffusion limit the intensity is written as the Legendre expansion  $I_\nu = J_\nu + 3H_\nu\mu$  with  $H_\nu \ll J_\nu$ , corresponding to the large scattering limit  $\tilde{r} \ll \tilde{\nu}$ , and thus we neglect the derivative  $\partial\tilde{H}/\partial\tilde{\nu}$  in the first order angular moment equation. The resulting diffusion relation between  $\tilde{H}$  and  $\tilde{J}$  is substituted into equation (C2) to obtain a single equation for  $\tilde{J}$ ; if we do this and change frequency variable to  $\sigma = \tilde{\nu}^3/9$  we obtain

$$\begin{aligned} \frac{\partial\tilde{J}}{\partial\sigma} - \frac{1}{\tilde{r}^2} \frac{\partial}{\partial\tilde{r}} \left( \tilde{r}^2 \frac{\partial\tilde{J}}{\partial\tilde{r}} \right) &= \frac{\delta(\tilde{r})}{(4\pi\tilde{r})^2} \times \frac{\delta(\tilde{\nu})}{(3\sigma^2)^{1/3}} \\ &= \frac{\delta(\tilde{r})}{(4\pi\tilde{r})^2} \times \delta(\sigma) \end{aligned} \quad (\text{C4})$$

where we have multiplied by the factor  $d\tilde{\nu}/d\sigma = (3\sigma^2)^{-1/3}$  in the first line and used  $\delta(\tilde{\nu}) = \delta(\sigma)/|d\tilde{\nu}/d\sigma|$  in the second. This equation is the diffusion equation in three dimensions with  $\sigma$  acting as the time variable and a point source impulse at  $\sigma = 0$ . The solution is given by (see Loeb & Rybicki's equation 21)

$$\tilde{J}(\tilde{r}, \tilde{\nu}) = \frac{1}{4\pi} \left( \frac{9}{4\pi\tilde{\nu}^3} \right)^{3/2} \exp\left(-\frac{9\tilde{r}^2}{4\tilde{\nu}^3}\right). \quad (\text{C5})$$

The corresponding flux, after using Loeb & Rybicki's solution for the mean intensity in the first order angular moment equation, is

$$\tilde{H}(\tilde{r}, \tilde{\nu}) = -\frac{\tilde{\nu}^2}{3} \frac{\partial\tilde{J}}{\partial\tilde{r}} = \frac{3\tilde{r}}{8\pi\tilde{\nu}} \left( \frac{9}{4\pi\tilde{\nu}^3} \right)^{3/2} \exp\left(-\frac{9\tilde{r}^2}{4\tilde{\nu}^3}\right). \quad (\text{C6})$$

## C2 Continuum Source

It is useful to consider the radiative transfer moment equations applicable in the zero temperature and diffusion limits for a source term of general frequency dependence  $s(\tilde{\nu})$ . The combined moment equation is given by equation (C4) with  $\delta(\tilde{\nu}) \rightarrow s(\tilde{\nu})$ . We use a Green's function approach to solve the combined moment equation by first considering a monochromatic source emitting at a single frequency  $\tilde{\nu}_s$  with  $s(\tilde{\nu}) = \delta(\tilde{\nu} - \tilde{\nu}_s) = (3\sigma^2)^{1/3} \delta(\sigma - \sigma_s)$  where  $\sigma_s = \tilde{\nu}_s^3/9$ . We label the solution as  $\tilde{G}(\tilde{r}, \sigma, \sigma_s)$ . The Green's function satisfies

$$\frac{\partial\tilde{G}}{\partial\sigma} - \frac{1}{\tilde{r}^2} \frac{\partial}{\partial\tilde{r}} \left( \tilde{r}^2 \frac{\partial\tilde{G}}{\partial\tilde{r}} \right) = \frac{\delta(\tilde{r})}{(4\pi\tilde{r})^2} \times \delta(\sigma - \sigma_s). \quad (\text{C7})$$

The solution is then the 3D diffusion solution for a point source impulse at  $\sigma = \sigma_s$ :

$$\tilde{G}(\tilde{r}, \sigma - \sigma_s) = \begin{cases} \frac{1}{4\pi} \left[ \frac{1}{4\pi(\sigma - \sigma_s)} \right]^{3/2} \exp\left[-\frac{\tilde{r}^2}{4(\sigma - \sigma_s)}\right]; & \sigma > \sigma_s \\ 0; & \sigma < \sigma_s \end{cases} \quad (\text{C8})$$

where the factor  $1/(4\pi)$  ensures unit source normalisation. Given  $\tilde{G}$ , the solution to the problem for a source of general frequency dependence satisfying equation (C4) with  $\delta(\tilde{\nu}) \rightarrow s(\tilde{\nu})$  is given by

$$\tilde{J}(\tilde{r}, \sigma) = \int_{-\infty}^{\infty} \tilde{G}(\tilde{r}, \sigma - \sigma_s) \frac{s(\sigma_s)}{(3\sigma_s^2)^{1/3}} d\sigma_s. \quad (\text{C9})$$

Thus we may construct the solution for a source of arbitrary frequency dependence from this result and equation (C8).

We now return to the case of a flat source spectrum as an approximation to the spectrum of a continuum source in

the IGM, for which the dimensionless source term has frequency dependence  $s(\tilde{\nu}) \rightarrow 1$ . It will be useful to specify a blue cutoff frequency  $\tilde{\nu}_m < 0$ , the maximum frequency (or minimum value of  $\tilde{\nu}$ ) at which the source emits photons capable of interacting with the Ly $\alpha$  line, giving a step-function form for the source frequency distribution:

$$s(\sigma) = \Theta(\sigma - \sigma_m) \equiv \begin{cases} 1 & ; \sigma > \sigma_m \\ 0 & ; \sigma \leq \sigma_m \end{cases} \quad (\text{C10})$$

where  $\sigma_m = \tilde{\nu}_m^3/9$ . We use the Green's function and the source frequency distribution to obtain the solution according to equation (C9), valid for  $\sigma > \sigma_m$ :

$$\begin{aligned} \tilde{J}(\tilde{r}, \sigma) &= \frac{1}{3^{1/3}} \int_{\sigma_m}^{\sigma} \sigma_s^{-2/3} \tilde{G}(\tilde{r}, \sigma - \sigma_s) d\sigma_s \\ &= \frac{1}{3^{1/3} (4\pi)^{5/2}} \int_{\sigma_m}^{\sigma} \frac{1}{\sigma_s^{2/3} (\sigma - \sigma_s)^{3/2}} \exp\left[-\frac{\tilde{r}^2}{4(\sigma - \sigma_s)}\right] d\sigma_s, \end{aligned} \quad (\text{C11})$$

$$\begin{aligned} \tilde{H}(\tilde{r}, \sigma) &= -\frac{\tilde{\nu}^2}{3^{4/3}} \frac{\partial}{\partial\tilde{r}} \int_{\sigma_m}^{\sigma} \sigma_s^{-2/3} \tilde{G}(\tilde{r}, \sigma - \sigma_s) d\sigma_s \\ &= \frac{\sigma^{2/3} \tilde{r}}{2(4\pi)^{5/2}} \int_{\sigma_m}^{\sigma} \frac{1}{\sigma_s^{2/3} (\sigma - \sigma_s)^{5/2}} \exp\left[-\frac{\tilde{r}^2}{4(\sigma - \sigma_s)}\right] d\sigma_s. \end{aligned} \quad (\text{C12})$$

The forms given by equations (49) and (50) are obtained with the change of variable  $u = 9\tilde{r}^2/[4(\tilde{\nu}^3 - \tilde{\nu}_s^3)]$ ; these latter forms are much easier to numerically integrate.

For  $\nu_m \rightarrow -\infty$ , equations (C11) and (C12) have the asymptotic series representations in  $t = -4\sigma/\tilde{r}^2$

$$\begin{aligned} \tilde{J}(\tilde{r}, t) &\sim \left(\frac{2^7}{3}\right)^{1/3} \frac{\Gamma(7/6)}{(4\pi)^{5/2}} \tilde{r}^{-7/3} \\ &\times \left[ 1 + \sum_{n=1}^{\infty} \frac{\Gamma(n+7/6)}{\Gamma(7/6)} b(-2/3, n) t^n \right] \end{aligned} \quad (\text{C13})$$

and

$$\begin{aligned} \tilde{H}(\tilde{r}, t) &\sim \left(\frac{2^5}{9}\right)^{2/3} \frac{\Gamma(13/6)}{(4\pi)^{5/2}} \tilde{r}^{-10/3} \tilde{\nu}^2 \\ &\times \left[ 1 + \sum_{n=1}^{\infty} \frac{\Gamma(n+13/6)}{\Gamma(13/6)} b(-2/3, n) t^n \right], \end{aligned} \quad (\text{C14})$$

for  $|t| \ll 1$ , noting the general series expansion

$$\begin{aligned} I_p(\tilde{r}, t) &\equiv \int_{-\infty}^{\sigma} d\sigma_s \sigma_s^{-2/3} (\sigma - \sigma_s)^{-p} e^{\sigma/[t(\sigma - \sigma_s)]} \\ &\sim \left(\frac{4}{\tilde{r}^2}\right)^{p-1/3} \sum_{n=0}^{\infty} b\left(-\frac{2}{3}, n\right) \Gamma\left(p + n - \frac{1}{3}\right) \end{aligned} \quad (\text{C15})$$

where  $b(-2/3, n)$  is a binomial coefficient  $(1, -2/3, 5/9, \dots)$ . For  $|t| \gg 1$ ,

$$I_p(\tilde{r}, t) \sim \left(\frac{4}{\tilde{r}^2}\right)^{p-1/3} \Gamma(p-1) t^{-2/3} \left(1 - \frac{2}{3} \frac{p-1}{t} \pm \dots\right), \quad (\text{C16})$$

where the number of terms retained in the bracketed sum does not exceed  $p$ . This gives the leading behaviours

$$\tilde{J}(\tilde{r}, t) \sim \left(\frac{2^7}{3}\right)^{1/3} \frac{1}{2(4\pi)^2} \tilde{r}^{-7/3} \frac{1}{t^{2/3}} \quad (\text{C17})$$

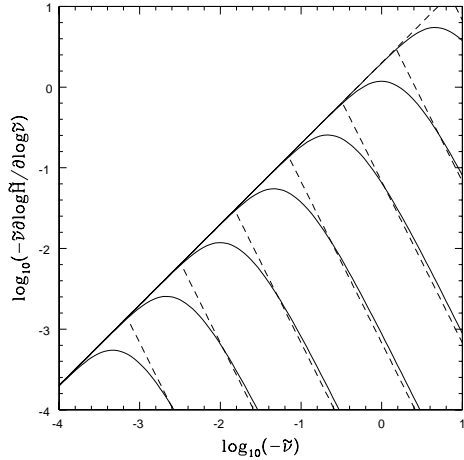


**Figure C1.** Solid lines: The ratio  $\tilde{\nu} \partial \log \tilde{H} / \partial \log \tilde{\nu}$  for various  $\tilde{r}$  ranging in decades from  $10^{-5}$  to 10 from bottom to top. Dashed lines: The ratio using the asymptotic expansions for  $|4\tilde{\nu}^3/9\tilde{r}^2| \ll 1$  and  $|4\tilde{\nu}^3/9\tilde{r}^2| \gg 1$ .

and

$$\tilde{H}(\tilde{r}, t) \sim \frac{1}{(4\pi\tilde{r})^2} \left(1 - \frac{1}{t}\right). \quad (\text{C18})$$

The diffusion approximation breaks down when  $\partial \tilde{H} / \partial \tilde{\nu}$  is no longer negligible compared with  $\tilde{H}/\tilde{\nu}^2$ . The approximations equations (C14) and (C18) may be used to estimate the radius at which the solution will fail. For  $|t| \ll 1$ ,  $\tilde{\nu} \partial \log \tilde{H} / \partial \log \tilde{\nu} \sim 2\tilde{\nu}$ , while for  $|t| \gg 1$ ,  $\tilde{\nu} \partial \log \tilde{H} / \partial \log \tilde{\nu} \sim -(27/4)(\tilde{r}/\tilde{\nu})^2$ . Equating these gives as an approximation for the value of the frequency at which  $|\tilde{\nu} \partial \log \tilde{H} / \partial \log \tilde{\nu}|$  peaks of  $\tilde{\nu}_{\text{peak}} \sim -(3/2)\tilde{r}^{2/3}$ , with a peak value of  $|\tilde{\nu} \partial \log \tilde{H} / \partial \log \tilde{\nu}|_{\text{peak}} \simeq 3\tilde{r}^{2/3}$ . Accordingly, the approximation is valid only for  $\tilde{r} \ll 1/3^{3/2}$ . Comparison with Fig. C1 shows the peak of  $|\tilde{\nu} \partial \log \tilde{H} / \partial \log \tilde{\nu}|$  exceeds 0.25 for  $\tilde{r} > 0.1$ , at which the diffusion approximation will begin to break down.

The solution obtained in Section 4.4 shows that while at large  $\tilde{r}$ ,  $|\tilde{\nu} \partial \log \tilde{H} / \partial \log \tilde{\nu}|$  approaches unity at large values of  $|\tilde{\nu}|$ , for  $|\tilde{\nu}| \ll 1$  the ratio is still small, so that  $\partial \tilde{H} / \partial \tilde{\nu}$  may continue to be neglected. Equations (C2) and (C3) then admit the similarity solution in  $t$  for  $|t| \ll 1$

$$\tilde{J}(\tilde{r}, t) = \frac{1}{(4\pi\tilde{r})^2} j(t), \quad (\text{C19})$$

$$\tilde{H}(\tilde{r}, t) = \frac{2}{3(4\pi)^2} \frac{\tilde{\nu}^2}{\tilde{r}^3} \left[ j(t) + t \frac{dj(t)}{dt} \right] \quad (\text{C20})$$

and  $\tilde{K} = \tilde{J}/3$ , where  $j(t) \sim (1 - \frac{1}{2}t + \frac{3}{4}t^2 - \frac{45}{24}t^3 \pm \dots)$ . This is found to agree well with the numerical solution obtained from the ray/moment method.

## APPENDIX D: TABLES OF TEST SUITE SOLUTIONS

Tables of the angle-averaged intensity of the radiation field computed using the ray and moment method are available

on-line for six test problems, as summarised here. Unless stated otherwise, the maximum frequency adopted for the continuum sources is  $x_m = 1000$ .

### D1 Test 1: Emission line source in a static medium

An analytic solution in the diffusion approximation is provided by Dijkstra et al. (2006). We provide two solutions for RII scattering, (a) in the Eddington approximation and (b) solving the full ray and moment equations. The solution using the full ray and moment equations is tabulated in Table D1. The results in the Eddington approximation are very similar.

### D2 Test 2: Emission line source in a uniformly expanding homogeneous medium

An analytic solution in the diffusion approximation is provided by Loeb & Rybicki (1999) as well as Monte Carlo code results. (Also see Appendix C.) We provide a solution for coherent scattering solving the full ray and moment equations. The results are tabulated in Table D2. (Vanishingly small values of  $\log_{10} \tilde{J}$  are indicated by a value of  $-100$ .)

### D3 Test 3: Continuum line source in a uniformly expanding homogeneous medium

An analytic solution in the diffusion approximation is provided in Appendix C. We provide three solutions, solving the full ray and moment equations for (a) coherent scattering, (b) RII redistribution, and (c) RII redistribution with recoils, all for a source upper frequency cutoff of  $x_m = 1000$ . An additional solution for RII redistribution with recoil is also provided with  $x_m = 1.4 \times 10^5$ , corresponding to Ly $\beta$ . A temperature of  $T = 10$  K is assumed for all solutions. The results are tabulated in Tables D3-D6.

### D4 Test 4: Continuum line source in a uniformly expanding medium with an overdense shell

The density profile is described by equation (62). We provide a solution for coherent scattering solving the full ray and moment equations. The results are tabulated in Table D7.

### D5 Test 5: Continuum line source in an expanding homogeneous medium with a quadratic velocity profile

The velocity profile is given by equation (63). We provide a solution for coherent scattering solving the full ray and moment equations. The results are tabulated in Table D8.

### D6 Test 6: Continuum line source in a medium with a self-consistent linear density and velocity perturbation around the source

The density and velocity perturbations are described by equations (64) and (65). We provide a solution for coherent scattering solving the full ray and moment equations, illustrated for both a linear perturbation with  $\Delta_0 = 0.5$

**Table D1.** Test 1:  $J(r, x)$  (in units of  $10^{-9}$ ) for Ly $\alpha$  source in homogeneous, static medium ( $T = 10$  K,  $\kappa_0 = 100$ ,  $r_S = 5$ ): RII redistribution

$x$	$r = 600$	$r = 650$	$r = 700$	$r = 750$	$r = 800$	$r = 850$	$r = 900$	$r = 950$	$r = 1000$
0.000	10.08642	7.96955	6.26884	4.87326	3.70389	2.70188	1.81926	1.00640	0.00030
0.100	10.08641	7.96955	6.26883	4.87325	3.70389	2.70188	1.81926	1.00640	0.00030
0.200	10.08642	7.96955	6.26884	4.87326	3.70389	2.70188	1.81926	1.00640	0.00031
0.300	10.08641	7.96955	6.26883	4.87325	3.70389	2.70188	1.81926	1.00640	0.00033
0.400	10.08642	7.96955	6.26884	4.87326	3.70389	2.70188	1.81926	1.00640	0.00035
0.500	10.08641	7.96955	6.26883	4.87325	3.70389	2.70188	1.81926	1.00640	0.00038

Note: The full table is published in the el

**Table D2.** Test 2:  $\log_{10} \tilde{J}(\tilde{r}, \tilde{\nu})$  for Ly $\alpha$  source in uniformly expanding homogeneous medium: coherent scattering

$\log_{10} \tilde{r}$	$\log_{10} \tilde{\nu} = -1.5$	$\log_{10} \tilde{\nu} = -1.0$	$\log_{10} \tilde{\nu} = -0.5$	$\log_{10} \tilde{\nu} = 0.0$	$\log_{10} \tilde{\nu} = 0.5$	$\log_{10} \tilde{\nu} = 1.0$	$\log_{10} \tilde{\nu} = 1.5$
-3.000	5.4131	3.2324	1.0482	-1.0900	-3.1419	-5.1395	-7.1773
-2.987	5.4119	3.2327	1.0483	-1.0899	-3.1419	-5.1395	-7.1773
-2.975	5.4103	3.2328	1.0484	-1.0899	-3.1419	-5.1395	-7.1773
-2.963	5.4085	3.2328	1.0484	-1.0899	-3.1418	-5.1395	-7.1773
-2.950	5.4064	3.2329	1.0485	-1.0898	-3.1418	-5.1395	-7.1773

Note: The full table is published in the electronic version of the paper. A portion is shown here only for guidance regarding its form and content.

**Table D3.** Test 3a:  $\log_{10} \tilde{J}(\tilde{r}, x)$  for continuum source in uniformly expanding homogeneous medium: coherent scattering

$x$	$\log_{10} \tilde{r} = -4.2$	$\log_{10} \tilde{r} = -3.9$	$\log_{10} \tilde{r} = -3.6$	$\log_{10} \tilde{r} = -3.3$	$\log_{10} \tilde{r} = -3.0$	$\log_{10} \tilde{r} = -2.7$	$\log_{10} \tilde{r} = -2.4$
-0.624	7.53670	6.84844	6.15478	5.45860	4.76086	4.05933	3.35097
-0.374	7.53669	6.84844	6.15478	5.45860	4.76086	4.05933	3.35097
-0.125	7.53668	6.84844	6.15478	5.45860	4.76086	4.05933	3.35097
0.125	7.53668	6.84844	6.15478	5.45860	4.76086	4.05933	3.35097
0.374	7.53667	6.84844	6.15478	5.45860	4.76086	4.05933	3.35097
0.624	7.53667	6.84844	6.15478	5.45860	4.76086	4.05933	3.35097

Note: The full table is published in the electronic version of the paper. A portion is shown here only for guidance regarding its form and content.

**Table D4.** Test 3b:  $\log_{10} \tilde{J}(\tilde{r}, x)$  for continuum source in uniformly expanding homogeneous medium: RII redistribution

$x$	$\log_{10} \tilde{r} = -4.2$	$\log_{10} \tilde{r} = -3.9$	$\log_{10} \tilde{r} = -3.6$	$\log_{10} \tilde{r} = -3.3$	$\log_{10} \tilde{r} = -3.0$	$\log_{10} \tilde{r} = -2.7$	$\log_{10} \tilde{r} = -2.4$
-1.248	7.58208	6.99331	6.36254	5.63254	4.82461	4.07154	3.36266
-0.749	7.58208	6.99330	6.36254	5.63255	4.82461	4.07154	3.36266
-0.250	7.58208	6.99331	6.36253	5.63254	4.82461	4.07154	3.36266
0.250	7.58208	6.99330	6.36254	5.63255	4.82461	4.07154	3.36266
0.749	7.58208	6.99331	6.36253	5.63254	4.82461	4.07154	3.36266
1.248	7.58208	6.99329	6.36254	5.63254	4.82461	4.07154	3.36266

Note: The full table is published in the electronic version of the paper. A portion is shown here only for guidance regarding its form and content.

**Table D5.** Test 3c:  $\log_{10} \tilde{J}(\tilde{r}, x)$  for continuum source in uniformly expanding homogeneous medium: RII redistribution with recoils

$x$	$\log_{10} \tilde{r} = -4.2$	$\log_{10} \tilde{r} = -3.9$	$\log_{10} \tilde{r} = -3.6$	$\log_{10} \tilde{r} = -3.3$	$\log_{10} \tilde{r} = -3.0$	$\log_{10} \tilde{r} = -2.7$	$\log_{10} \tilde{r} = -2.4$
-1.248	7.56362	6.94959	6.28331	5.51825	4.70934	3.97269	3.26682
-0.749	7.56013	6.94608	6.27983	5.51476	4.70586	3.96920	3.26333
-0.250	7.55665	6.94262	6.27634	5.51128	4.70237	3.96572	3.25985
0.250	7.55316	6.93911	6.27286	5.50780	4.69889	3.96223	3.25636
0.749	7.54968	6.93565	6.26937	5.50431	4.69541	3.95875	3.25288
1.248	7.54619	6.93215	6.26589	5.50083	4.69192	3.95526	3.24939

Note: The full table is published in the electronic version of the paper. A portion is shown here only for guidance regarding its form and content.



**Table D6.** Test 3d:  $\log_{10} \tilde{J}(\tilde{r}, x)$  for continuum source in uniformly expanding homogeneous medium: RII redistribution with recoil for  $x_m = 1.4 \times 10^5$ 

$x$	$\log_{10} \tilde{r} = -2.9$	$\log_{10} \tilde{r} = -2.2$	$\log_{10} \tilde{r} = -1.5$	$\log_{10} \tilde{r} = -0.8$	$\log_{10} \tilde{r} = -0.1$	$\log_{10} \tilde{r} = 0.6$	$\log_{10} \tilde{r} = 1.3$
-2.488	4.46782	2.82518	1.21451	-0.40622	-1.94001	-3.42438	-4.87538
-1.493	4.46080	2.81814	1.20748	-0.41326	-1.94704	-3.43141	-4.88241
-0.498	4.45394	2.81130	1.20064	-0.42010	-1.95388	-3.43825	-4.88925
0.498	4.44692	2.80426	1.19359	-0.42714	-1.96093	-3.44530	-4.89630
1.493	4.44006	2.79743	1.18676	-0.43398	-1.96776	-3.45213	-4.90313
2.488	4.43304	2.79038	1.17971	-0.44102	-1.97481	-3.45917	-4.91018

Note: The full table is published in the electronic version of the paper. A portion is shown here only for guidance regarding its form and content.

**Table D7.** Test 4:  $\log_{10} \tilde{J}(\tilde{r}, x)$  for continuum source in uniformly expanding medium with overdense shell: coherent scattering

$x$	$\log_{10} \tilde{r} = -4.2$	$\log_{10} \tilde{r} = -3.9$	$\log_{10} \tilde{r} = -3.6$	$\log_{10} \tilde{r} = -3.3$	$\log_{10} \tilde{r} = -3.0$	$\log_{10} \tilde{r} = -2.7$	$\log_{10} \tilde{r} = -2.4$
-0.855	7.55695	6.94865	6.53139	5.85581	5.07235	4.25632	3.03729
-0.513	7.55693	6.94865	6.53139	5.85581	5.07235	4.25632	3.03729
-0.171	7.55692	6.94864	6.53139	5.85581	5.07235	4.25632	3.03729
0.171	7.55692	6.94864	6.53139	5.85581	5.07235	4.25632	3.03729
0.513	7.55691	6.94864	6.53139	5.85581	5.07235	4.25632	3.03729
0.855	7.55691	6.94864	6.53139	5.85581	5.07235	4.25632	3.03729

Note: The full table is published in the electronic version of the paper. A portion is shown here only for guidance regarding its form and content.

and extended into the non-linear regime with  $\Delta_0 = 2.9$  (the latter case is not a fully self-consistent cosmological perturbation). The results are tabulated in Tables D9 and D10.

## ACKNOWLEDGMENTS

## REFERENCES

- Auer L. H., 1971, *Journal of Quantitative Spectroscopy and Radiative Transfer*, 11, 573
- Baek S., Di Matteo P., Semelin B., Combes F., Revaz Y., 2009, *A&A*, 495, 389
- Basko M. M., 1978, *Zhurnal Eksperimental noi i Teoreticheskoi Fiziki*, 75, 1278
- Bouwens R. J., Illingworth G. D., Labbe I., Oesch P. A., Trenti M., Carollo C. M., van Dokkum P. G., Franx M., Stiavelli M., González V., Magee D., Bradley L., 2011, *Nature*, 469, 504
- Chen X., Miralda-Escudé J., 2004, *ApJ*, 602, 1
- Chuzhoy L., Zheng Z., 2007, *ApJ*, 670, 912
- Dijkstra M., Haian Z., Spaans M., 2006, *ApJ*, 649, 14
- Field G. B., 1958, *Proc. I.R.E.*, 46, 240
- Field G. B., 1959a, *ApJ*, 129, 536
- Field G. B., 1959b, *ApJ*, 129, 551
- Furlanetto S. R., Pritchard J. R., 2006, *MNRAS*, 372, 1093
- Harrington J. P., 1973, *MNRAS*, 162, 43
- Higgins J., 2012, PhD thesis, Univ. Edinburgh
- Higgins J., Meiksin A., 2009, *MNRAS*, 393, 949
- Komatsu E., Smith K. M., Dunkley J., Bennett C. L., Gold B., Hinshaw G., Jarosik N., Larson D., Nolte M. R., Page L., Spergel D. N., Halpern M., 2011, *ApJS*, 192, 18
- Loeb A., Rybicki G. B., 1999, *ApJ*, 524, 527
- Lucy L. B., 1999, *A&A*, 344, 282
- Madau P., Meiksin A., Rees M. J., 1997, *ApJ*, 475, 429
- McLure R. J., Dunlop J. S., de Ravel L., Cirasuolo M., Ellis R. S., Schenker M., Robertson B. E., Koekemoer A. M., Stark D. P., Bowler R. A. A., 2011, *MNRAS*, 418, 2074
- Mihalas D., 1978, *Stellar atmospheres* (2nd edition). San Francisco, W. H. Freeman and Co., 1978.
- Mihalas D., Kunasz P. B., Hummer D. G., 1975, *ApJ*, 202, 465
- Mihalas D., Kunasz P. B., Hummer D. G., 1976, *ApJ*, 210, 419
- Mihalas D., Kunasz P. B., Hummer D. G., 1977, *ApJ*, 214, 337
- Ono Y., Ouchi M., Mobasher B., Dickinson M., Penner K., Shimasaku K., Weiner B. J., Kartaltepe J. S., Nakajima K., Nayyeri H., Stern D., Kashikawa N., Spinrad H., 2012, *ApJ*, 744, 83
- Pritchard J. R., Loeb A., 2011, *ArXiv e-prints*, 1109.6012
- Roy I., Xu W., Qiu J.-M., Shu C.-W., Fang L.-Z., 2009a, *ApJ*, 694, 1121
- Roy I., Xu W., Qiu J.-M., Shu C.-W., Fang L.-Z., 2009b, *ApJ*, 703, 1992
- Rybicki G. B., dell’Antonio I. P., 1994, *ApJ*, 427, 603
- Schenker M. A., Stark D. P., Ellis R. S., Robertson B. E., Dunlop J. S., McLure R. J., Kneib J.-P., Richard J., 2012, *ApJ*, 744, 179
- Semelin B., Combes F., Baek S., 2007, *A&A*, 474, 365
- Tasitsiomi A., 2006, *ApJ*, 645, 792
- Vanzella E., Pentericci L., Fontana A., Grazian A., Castellano M., Boutsia K., Cristiani S., Dickinson M., Gallozzi S., Giallongo E., Giallisco M., Maiolino R., Moorwood A., Paris D., Santini P., 2011, *ApJ*, 730, L35
- Vonlanthen P., Semelin B., Baek S., Revaz Y., 2011, *A&A*, 532, A97
- Wouthuysen S. A., 1952, *AJ*, 57, 31

**Table D8.** Test 5:  $\log_{10} \tilde{J}(\tilde{r}, x)$  for continuum source in homogeneous medium with quadratic velocity profile: coherent scattering

$x$	$\log_{10} \tilde{r} = -4.1$	$\log_{10} \tilde{r} = -3.8$	$\log_{10} \tilde{r} = -3.5$	$\log_{10} \tilde{r} = -3.2$	$\log_{10} \tilde{r} = -2.9$	$\log_{10} \tilde{r} = -2.6$	$\log_{10} \tilde{r} = -2.3$
-0.997	7.80416	7.26099	6.64381	5.91760	5.09385	4.21712	3.30071
-0.598	7.80408	7.26095	6.64379	5.91760	5.09385	4.21712	3.30071
-0.199	7.80405	7.26094	6.64379	5.91760	5.09385	4.21712	3.30071
0.199	7.80403	7.26093	6.64378	5.91760	5.09385	4.21712	3.30071
0.598	7.80401	7.26092	6.64378	5.91760	5.09385	4.21712	3.30071
0.997	7.80399	7.26091	6.64378	5.91759	5.09385	4.21712	3.30071

Note: The full table is published in the electronic version of the paper. A portion is shown here only for guidance regarding its form and content.

**Table D9.** Test 6a:  $\log_{10} \tilde{J}(\tilde{r}, x)$  for continuum source in perturbed expanding medium ( $\Delta_0 = 0.5$ ): coherent scattering

$x$	$\log_{10} \tilde{r} = -3.0$	$\log_{10} \tilde{r} = -2.5$	$\log_{10} \tilde{r} = -2.0$	$\log_{10} \tilde{r} = -1.5$	$\log_{10} \tilde{r} = -1.0$	$\log_{10} \tilde{r} = -0.5$	$\log_{10} \tilde{r} = 0.0$
-2.488	4.86634	3.70669	2.54773	1.39233	0.21623	-0.93978	-2.12461
-1.493	4.86612	3.70667	2.54773	1.39233	0.21623	-0.93978	-2.12461
-0.498	4.86612	3.70667	2.54773	1.39233	0.21623	-0.93978	-2.12461
0.498	4.86612	3.70667	2.54773	1.39233	0.21623	-0.93978	-2.12461
1.493	4.86612	3.70667	2.54773	1.39233	0.21623	-0.93978	-2.12461
2.488	4.86612	3.70667	2.54773	1.39233	0.21623	-0.93978	-2.12461

Note: The full table is published in the electronic version of the paper. A portion is shown here only for guidance regarding its form and content.

Zheng Z., Miralda-Escudé J., 2002, ApJ, 578, 33

**Table D10.** Test 6b:  $\log_{10} \tilde{J}(\tilde{r}, x)$  for continuum source in perturbed expanding medium ( $\Delta_0 = 2.9$ ): coherent scattering

$x$	$\log_{10} \tilde{r} = -3.0$	$\log_{10} \tilde{r} = -2.5$	$\log_{10} \tilde{r} = -2.0$	$\log_{10} \tilde{r} = -1.5$	$\log_{10} \tilde{r} = -1.0$	$\log_{10} \tilde{r} = -0.5$	$\log_{10} \tilde{r} = 0.0$
-2.488	5.92320	4.76664	3.60367	2.43260	1.21809	-0.20383	-1.97424
-1.493	5.92113	4.76643	3.60365	2.43260	1.21809	-0.20383	-1.97424
-0.498	5.92111	4.76642	3.60365	2.43260	1.21809	-0.20383	-1.97424
0.498	5.92111	4.76642	3.60365	2.43260	1.21809	-0.20383	-1.97424
1.493	5.92111	4.76642	3.60365	2.43260	1.21809	-0.20383	-1.97424
2.488	5.92111	4.76642	3.60365	2.43260	1.21809	-0.20383	-1.97424

Note: The full table is published in the electronic version of the paper. A portion is shown here only for guidance regarding its form and content.